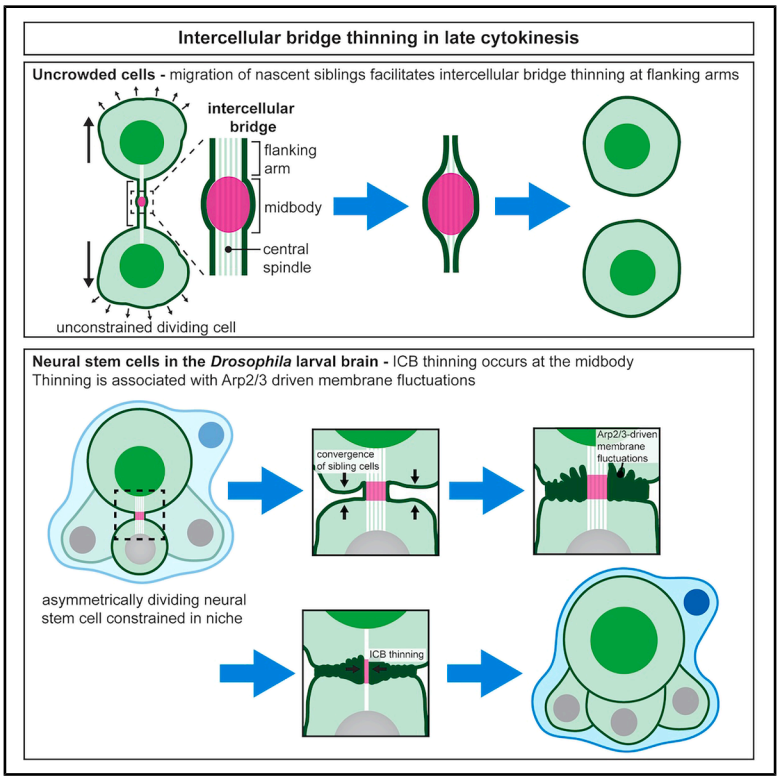
iScience

Article

Arp2/3 involvement in intercellular bridge membrane fluctuations and constriction during neural stem cell divisions

Graphical abstract



Highlights

- NSC intercellular bridges lack flanking arms and undergo thinning at the midbody
- Plasma membrane sheets fluctuate near the ICB during its constriction
- Arp2/3 localizes to fluctuating membrane sheets surrounding the ICB
- Arp2/3 inhibition reduces membrane fluctuations and slows ICB thinning

Authors

Bryce LaFoya, Michelle N. Ortman, Adam Fries, Brad J. Nolen, Kenneth E. Prehoda

Correspondence

lafoya@wisc.edu (B.L.), prehoda@uoregon.edu (K.E.P.)

In brief

Molecular biology; Neuroscience; Cell biology

LaFoya et al., 2026, iScience *29*, 115430
April 17, 2026 © 2026 The Author(s). Published by Elsevier Inc.
https://doi.org/10.1016/j.isci.2026.115430

CellPress

iScience

CellPress
OPEN ACCESS

Article

Arp2/3 involvement in intercellular bridge membrane fluctuations and constriction during neural stem cell divisions

Bryce LaFoya,[1,*] Michelle N. Ortman,[1] Adam Fries,[2] Brad J. Nolen,[1] and Kenneth E. Prehoda[1,3,*]
[1]Institute of Molecular Biology, University of Oregon, Department of Chemistry and Biochemistry, 1229 University of Oregon, Eugene, OR 97403, USA
[2]Genomics and Cell Characterization Core, University of Oregon, 1229 University of Oregon, Eugene, OR 97403, USA
[3]Lead contact
*Correspondence: lafoya@wisc.edu (B.L.), prehoda@uoregon.edu (K.E.P.)
https://doi.org/10.1016/j.isci.2026.115430

SUMMARY

Near the end of animal cell division, the nascent sibling cells remain connected by an intercellular bridge (ICB). The ICB must undergo constriction or thinning before the final step of cytokinetic abscission can occur. The canonical ICB has a central midbody surrounded by flanking regions that are thinned by the migration of nascent siblings away from one another. We studied ICB thinning during the asymmetric divisions of neural stem cells (NSCs), which take place in the complex environment of the *Drosophila* larval brain. We found that unlike the ICBs of uncrowded cultured cells, NSC ICBs lack flanking arms and instead thin at the midbody region. Super-resolution, full volume imaging revealed fluctuating plasma membrane sheets surrounding the ICB. Inhibition of the branched actin filament nucleator, the Arp2/3 complex, reduces membrane fluctuations and appears to impair ICB thinning. Our results indicate that dynamic, branched actin networks facilitate ICB-associated membrane remodeling and thinning.

INTRODUCTION

Cytokinesis in animal cells consists of three distinct plasma membrane constriction phases: furrowing, intercellular bridge (ICB) thinning, and abscission.[1,2] First, a broad actomyosin contractile ring forms a cleavage furrow between the segregated chromosomes, rapidly driving plasma membrane ingression until the furrow reaches a diameter of 1.5 μm.[3] In the second phase, central spindle microtubules are compacted within the furrow, and the structure reorganizes into the ICB and undergoes thinning.[4,5] When the ICB thins to approximately 200 nm in diameter, the final phase of cytokinesis occurs, where abscission severs the plasma membrane connection.[6] The ICB diameter must reach 200 nm before abscission can occur, and the initial furrowing phase ends at a diameter of 1.5 μm; therefore, ICB thinning is essential for the completion of cytokinesis. While ICB thinning is a crucial intermediary phase in cytokinesis, current models for thinning are based on observations of uncrowded cells in cultures (canonical ICBs, hereafter), and less is known about the process for cells that are part of a tissue.

Thinning of canonical ICBs is mediated by the migration of the nascent sibling cells away from one another.[4,5,7] Migration causes both thinning and lengthening of the ICB such that canonical ICBs can easily exceed 10 μm in length,[8–10] forming a tripartite organization with a central midbody flanked by two arms (in an alternate nomenclature, the terms ICB and midbody are sometimes used interchangeably, with the central region also referred to as the Flemming body or stem body).[6,10,11] The midbody contains the overlapping region of central spindle microtubules and is marked by specific microtubule binding proteins such as PRC1 and Centralspindlin.[12–17] The migration of the nascent sibling cells generates pulling forces that constrict the flanking arms of canonical ICBs, while leaving a thicker midbody region (Figure 1A). ICB thinning can also require other processes, such as microtubule disassembly.[18,19] It is not clear how ICB thinning occurs in tissue environments, however, where the spatial limitations posed by nearby cells and the extracellular matrix may prevent the large-scale movements used by dividing cultured cells.

To investigate how the ICB is thinned in dividing cells that reside in a tissue, we examined the ICB formed by asymmetrically dividing neural stem cells (NSCs; a.k.a. neuroblasts) of the larval *Drosophila* brain (Figure 1B). NSCs divide rapidly, generating a larger self-renewed stem cell and a smaller neural progenitor (NP).[20,21] The initial actomyosin-based furrowing phase of cytokinesis in NSCs is well characterized, with both spindle- and polarity-dependent signals positioning the actomyosin contractile ring.[22–27] As this first phase of cytokinesis concludes, cortical actomyosin flows are directed away from the furrow.[28] While the initial phase of NSC cytokinesis has been intensively studied, very little is known about late cytokinesis, and, importantly, the ICB thinning process in NSCs is uncharacterized. We investigated NSC ICB thinning with the goal of

This is an open access article under the CC BY-NC-ND license (http://creativecommons.org/licenses/by-nc-nd/4.0/).

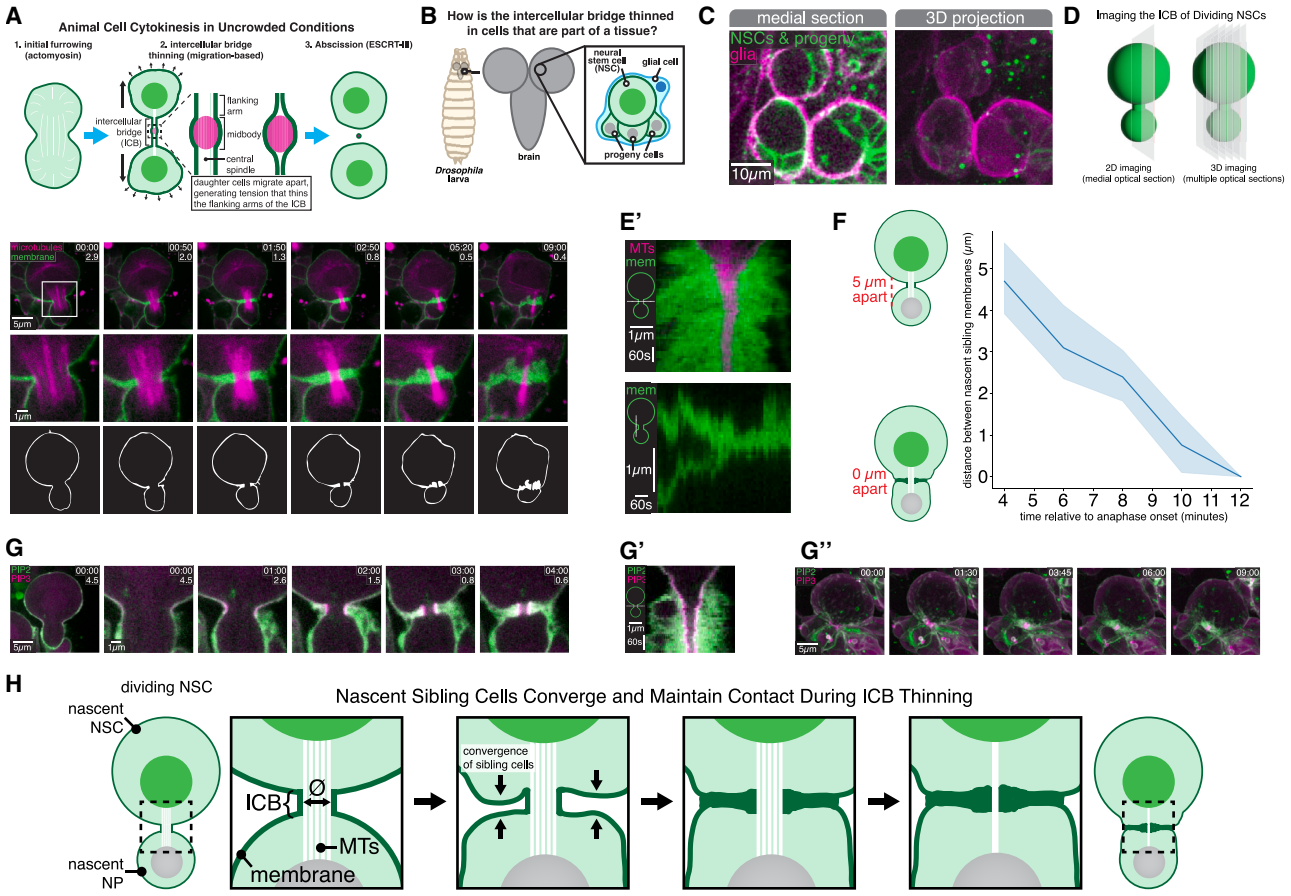


Figure 1. Examining tissue-constrained ICB thinning in *Drosophila* NSCs reveals differences in nascent sibling cell movements and ICB structure

(A) Cytokinesis in animal cell division consists of three main phases: furrowing, ICB thinning, and abscission. In the first phase, an actomyosin contractile ring constricts the cleavage furrow to approximately 1.5 μm. At this point, the ICB forms and begins to constrict in a process referred to as thinning. In uncrowded cultured cells, ICB thinning is driven by the movement of nascent sibling cells apart from each other, causing the ICB to narrow at the flanking arms and resulting in a central bulge known as the midbody. ICB thinning results in the ICB to undergo thinning to approximately 200 nm, which allows for the final phase known as abscission, where ESCRT-III severs the membrane connection.

(B) *Drosophila* NSCs are part of a complex tissue. In the larval *Drosophila* brain, NSCs divide in a constrained environment, surrounded by a cortex glial cell and smaller cells known as NPs, the NSC's progeny from previous NSC divisions. This study used the NSC as a model system for understanding how ICB thinning occurs in cells that are part of a tissue, where mechanical constraints may preclude the thinning mechanisms used by uncrowded cultured cells.

(C) *Drosophila* larval brain NSCs are surrounded by other cells. Glia (marked by Nrv2; magenta) and their progeny (marked by PLCδ-PH-mCherry; green) are shown in medial optical section and a 3D projection. Scale bars: 10 μm.

(D) Schematic of the imaging approaches used in this study to examine ICB dynamics in dividing NSCs. The NSC divides asymmetrically to yield a large sibling cell and a small sibling cell. 2D imaging of the ICB was performed using a single medial optical section. 3D reconstructions of the ICB were made using multiple optical sections from across the ICB.

(E) Membrane and microtubule dynamics during the late stages of NSC division. Dynamics of the microtubule marker Jupiter-mCherry and the plasma membrane marker Farnesyl-GFP are shown in a medial section of the entire dividing NSC (top row; scale bars, 5 μm), close-up view of ICB (middle row; scale bars, 1 μm), and manual segmentation (bottom row; scale bars, 5 μm), with frames selected from Video S1. Time relative to the start of imaging is indicated (mm:ss), along with the diameter of the cleavage furrow and subsequent ICB in microns to track the progress of cytokinesis.

(E′) A kymograph of membrane (mem) and MT dynamics across the cytokinetic furrow as the ICB forms and undergoes thinning (top row). A kymograph demonstrating that, as the ICB forms, nascent sibling cells rapidly come in contact and remain in contact with one another as the ICB thins (bottom row). Scale bars: 1 μm and 60 s.

(F) The distance between nascent sibling cells decreases during ICB thinning. Using movies of dividing NSCs expressing the membrane marker PLCδ-PH-GFP, a straight line was drawn along the division axis from the edge of the nascent NP to the membrane of the nascent NSC to measure the separation. The measured distances (microns) are plotted on *x* axis, and time (minutes) relative to anaphase onset is on *y* axis. The mean distances between nascent siblings ($n = 5$; $N = 3$) are shown, with standard deviations indicated by the shaded region around the trend line. During ICB thinning, sister cells move closer together and eventually adhere.

(G) Phosphoinositide dynamics during the late stages of NSC division. Dynamics of the PIP3 sensor GRP1-PH-GFP and the PIP2 sensor PLCδ-PH-mCherry are shown in medial sections (selected frames from Video S1). Time relative to the start of imaging is indicated (mm:ss), along with the diameter of the cleavage furrow and subsequent ICB in microns. Scale bars: 5 μm (first image) and 1 μm (following images).

(legend continued on next page)

determining whether it follows the canonical ICB thinning model that is derived from observations of uncrowded cultured cells.

RESULTS

The NSC ICB is a constricting midbody that lacks conventional flanking arms

Larval *Drosophila* brain NSCs divide in a highly constrained environment, surrounded on one side by a cluster of progeny cells from previous asymmetric divisions and on the other side by a cortex glial cell that envelops the NSCs and their progeny (Figures 1B and 1C). Using super-resolution microscopy, we observed the formation of the NSC ICB when the contractile ring constricted to approximately 1.5 μm, at which point the broad cleavage furrow reorganized into a cylindrical membrane containing a dense bundle of microtubules (Figure 1E).

While the nascent siblings of dividing, uncrowded cultured cells migrate away from one another during ICB thinning,[4,5,7] the nascent NSC siblings were found to move toward one another (Figure 1E and Video S1). The gap between the nascent sibling cells following the formation of the ICB disappeared as they moved toward one another and made contact (Figure 1F, $n = 5$; $N = 3$). Contact between the NSC and NP siblings has been previously described,[29,30] and our data demonstrate that these contacts are made well before the division completes. The contacts between the NSC-NP siblings are phosphatidylinositol (3,4,5)-trisphosphate (PIP3)-based cadherin adhesions,[29] and we observed a dramatic enrichment of phosphatidylinositol (3,4,5)-trisphosphate (PIP3) lipids in the membrane of the cleavage furrow as it reorganized into the cylindrical ICB structure (Figure 1G and Video S1).

Canonical ICBs feature a central midbody marked by the presence of proteins such as Centralspindlin.[10] To learn more about the structure of the NSC ICB, we performed dual imaging of the plasma membrane and the Centralspindlin component Pavarotti (Pav; MKLP1 in vertebrates)[16,17] Comparing the height of the cylinder wall of the ICB with the span of the ICB marked by Pavarotti revealed no difference (Figures 2A–2C and Video S2), indicating that flanking arms were not detectable in the ICB (Figure 2D). The lack of detectable flanking arms suggests that ICB thinning occurs by a different mechanism in NSCs. Consistent with this possibility, we observed thinning in the Pavarotti-marked region of the ICB (i.e., at the midbody). In canonical ICBs, the contractile ring component Anillin forms rings on the flanking arms where it mediates constriction.[31,32] In NSCs, we observed that Anillin is uniformly distributed along the ICB cylinder wall and that the entire structure undergoes uniform thinning (Figures 2E–2H and Video S2). Together, these results indicate that dividing NSCs form an ICB that consists solely of a midbody that undergoes thinning (Figure 2I).

Sheets of the plasma membrane fluctuate near the ICB during its formation and constriction

We found that NSCs and uncrowded cultured cells have key differences in their ICB structures and in how their nascent sibling cells move relative to one another. These differences prompted us to explore the underlying mechanisms of NSC ICB thinning. Plasma membrane remodeling at the NSC-NP interface has been reported to occur near the end of division.[30,33–35] We speculated that membrane remodeling could be related to the mechanisms that thin the ICB in NSCs.

To investigate membrane remodeling and its relationship with ICB formation and thinning, we performed dual imaging of the plasma membrane and microtubules, capturing images across the entire volume of the ICB, which allowed us to generate 3D projections of the structure. We observed highly dynamic membrane remodeling that commenced as the cleavage furrow reorganized into the ICB (Figure 3A and Video S3). The plasma membrane surrounding the ICB fluctuated, leading to the accumulation of large (>1 μm) membrane sheets. The membrane sheets were most apparent in the larger nascent NSC sibling, although the smaller NP sibling cytoplasm could obscure their presence. The fluctuations contributed to a significant and rapid accumulation of plasma membrane around the ICB (Figure 3C). Thus, ICB thinning is associated with dramatic remodeling of the plasma membrane, characterized by fluctuations of the membrane near the ICB (Figure 3B).

ICB-associated plasma membrane fluctuations are driven by F-actin

The furrow cytoskeleton is dramatically remodeled during the transition from initial furrowing to ICB formation in NSCs,[28] with significant accumulation of F-actin.[35] We imaged F-actin alongside the plasma membrane to investigate the role of the actin cytoskeleton in ICB dynamics. We observed a large burst of F-actin near the ICB upon its initial formation that ultimately surrounded the fluctuating plasma membrane sheets (Figures 4A and 4B; Video S4). F-actin continued to surround the membrane sheets during ICB thinning. In addition to being localized near the membrane sheets, F-actin was also present at the ICB cylinder wall. To determine whether F-actin is required for membrane fluctuations and ICB thinning, we treated NSCs with the F-actin depolymerizing agent latrunculin A (LatA). The addition of LatA immediately after ICB formation halted the membrane fluctuations and prevented further thinning of the ICB (Figure 4C and Video S4). In contrast, NSCs treated with vehicle alone (DMSO) were unperturbed, exhibiting both membrane fluctuations and ICB thinning (Figure 4D and Video S4).

We examined the localization of distinct actin regulators to determine which of them might be responsible for ICB-associated F-actin. First, to determine if the ICB-associated actin

(G′) A kymograph of PIP3 and PIP2 dynamics across the ICB. Scale bars: 1 μm and 60 s.
(G″) 3D projections of PIP3 and PIP2 dynamics during the late stages of NSC division. Scale bars: 5 μm.
(H) Summary of nascent cell and ICB dynamics in NSCs. Unlike in uncrowded cultured cells, where ICB thinning occurs as nascent sibling cells move apart, the nascent sibling cells converge and adhere to one another during NSC ICB thinning. This contrast highlights a significant gap in our understanding of how ICB thinning occurs in cells packed within tissues, and nascent sibling cells do not move apart. Abbreviations: ICB, intercellular bridge; MTs, microtubules; NPs, neural progenitors; NSC, neural stem cell; Ø, diameter of ICB.

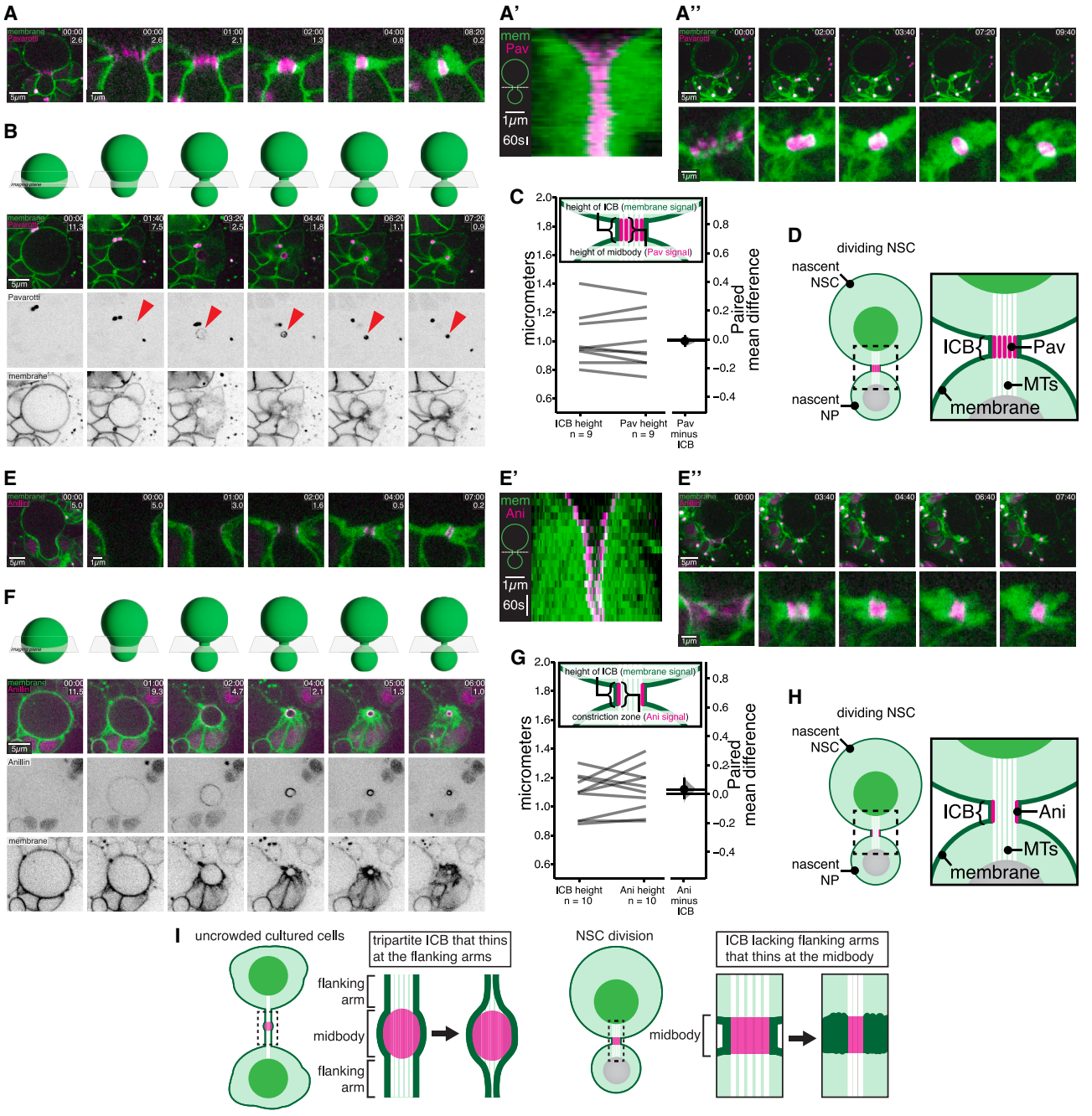


Figure 2. The NSC ICB lacks flanking arms and constricts at the midbody

(A) Pavarotti (Pav) and membrane dynamics during the late stages of NSC division. The dynamics of the Centralspindlin component Pav-GFP and the membrane marker PLCδ-PH-mCherry are shown in a medial section of the entire dividing NSC (first image) along with close-up views of the cleavage furrow (in the remaining images) (selected frames from Video S2). Time relative to the start of imaging is indicated (mm:ss), along with the diameter of the cleavage furrow and subsequent ICB in microns. Scale bars: 5 μm (first image) and 1 μm (following images). (A′) A kymograph of Pav and membrane (mem) dynamics across the ICB. Scale bars: 1 μm and 60 s. (A″) 3D projections of Pav and membrane dynamics during late NSC division for the entire dividing NSC (top row; scale bars, 5 μm) and a close-up of the cleavage furrow (bottom row; scale bars, 1 μm), with time relative to the start of imaging indicated (mm:ss).

(B) Pav and membrane dynamics during NSC division are shown from a perspective of the cleavage furrow and subsequent ICB as it constricts (selected frames from Video S2). Time relative to the start of imaging is indicated (mm:ss), along with the diameter of the cleavage furrow and subsequent ICB in microns. Scale bars: 5 μm.

(C) The NSC consists of a midbody without detectable flanking arms. The heights of the ICB and midbody were measured in dividing NSCs (n = 9; N = 9 brains) expressing the membrane marker PLCδ-PH-mCherry and the Centralspindlin marker Pav-GFP, which labels the midbody. These measurements were taken when the cleavage furrow reached approximately 1.5 μm in diameter. The paired mean difference between the heights of the ICB and the Pav-occupied region is

(legend continued on next page)

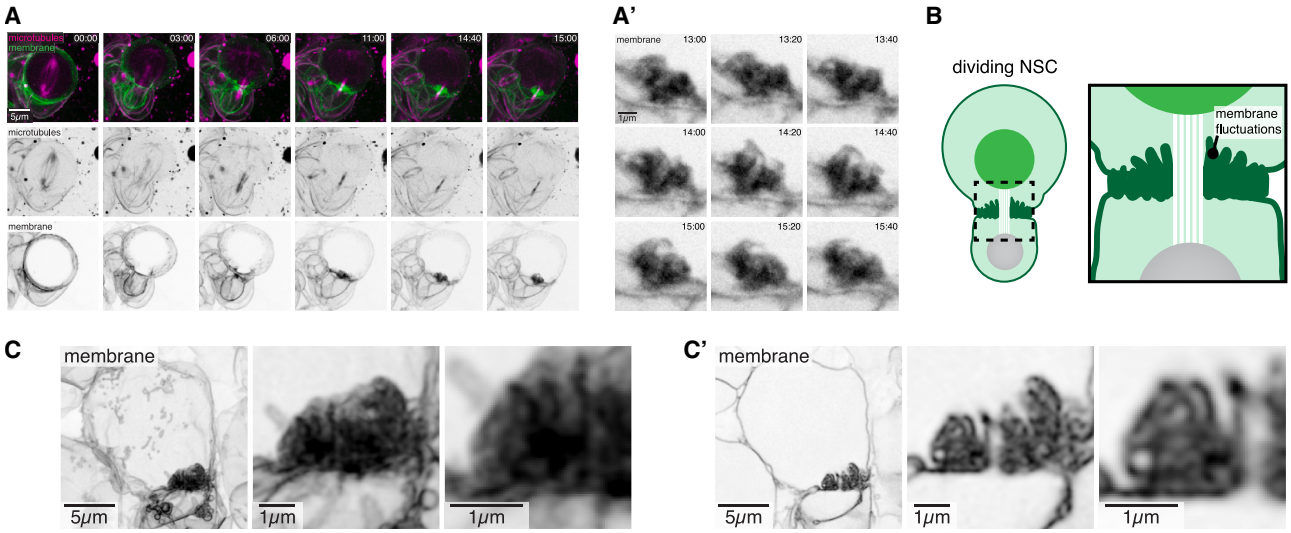


Figure 3. Dynamic plasma membrane structures surround the ICB as it thins

(A) Microtubules and membrane dynamics during the late stages of NSC division. Dynamics of the microtubule marker Jupiter-mCherry and the plasma membrane marker Farnesyl-GFP are shown in 3D projections (selected frames from Video S3). Time relative to the start of imaging is indicated (mm:ss). The NSC is expressing the microtubule marker Jupiter-mCherry and membrane marker Farnesyl-GFP. Scale bars: 5 μm.

(A′) A close-up view of the plasma membrane near the ICB highlights an example membrane fluctuation. Selected frames from Video S3 capture a time lapse of 3D projections. Scale bars: 1 μm.

(B) Schematic of plasma membrane accumulations near the ICB as it thins.

(C) Membrane accumulation around the ICB. A 3D projection of a dividing NSC expressing PLCδ-PH-GFP is shown alongside close-up views of the ICB-associated membrane structure (selected images from Video S3). Scale bars: 5 μm (left), 1 μm (center), and 1 μm (right).

(C′) The corresponding medial sections are displayed. Scale bars: 5 μm (left), 1 μm (center), and 1 μm (right).

cytoskeleton is a contractile network, we simultaneously tracked the motor protein Myosin II and F-actin. Myosin II was broadly distributed on the furrow cortex during the initial furrowing phase but dissipated from the furrow late in the process (Figure 5A and Video S5), as previously described.[28] Our data reveal that the loss of Myosin II in the broad furrow occurs at the onset of ICB formation. Concomitant with the loss of broad furrow Myosin II, its strong enrichment was observed on the ICB cylinder wall. However, we did not detect Myosin II within the dense actin network associated with the plasma membrane sheets adjacent

shown in a Gardner-Altman estimation plot. Both groups are plotted on the left axes as a slope graph: each paired set of observations is connected by a line. The paired mean difference is plotted on floating axes on the right as a bootstrap sampling distribution. The mean difference is depicted as a dot; the 95% confidence interval is indicated by the ends of the vertical error bar.

(D) Schematic of NSC ICB structure.

Abbreviations: ICB, intercellular bridge; MTs, microtubules; NP, neural progenitor; NSC, neural stem cell; Pav, Pavarotti.

(E) Anillin (Ani) and membrane dynamics during the late stages of NSC division. The dynamics of Ani-GFP and the membrane marker PLCδ-PH-mCherry are shown in a medial section of the entire dividing NSC (first image), along with a close-up view of the cleavage furrow during late cytokinesis (remaining images) (selected frames from Video S2). Time relative to the start of imaging is indicated (mm:ss), along with the diameter of the cleavage furrow and subsequent ICB in microns. Scale bars: 5 μm.

(E′) A kymograph of Ani and membrane (mem) dynamics across the ICB. Scale bars: 1 μm and 60 s.

(E″) 3D projections of Ani and membrane dynamics during the late stages of NSC division. Selected frames from Video S2 are shown. Top: entire dividing NSC (scale bars: 5 μm). Bottom: a close-up of the cleavage furrow (scale bars: 1 μm); time relative to the start of imaging is indicated (mm:ss).

(F) Ani and membrane dynamics during NSC division from a perspective looking into the cleavage furrow and subsequent ICB as it constricts (selected frames from Video S2). Time relative to the start of imaging is indicated (mm:ss), along with the diameter of the cleavage furrow and subsequent ICB in microns.

(G) NSC ICB thinning occurs at the midbody. Heights of the ICB and the constriction zone were measured in dividing NSCs (n = 10; N = 10 brains) expressing the membrane marker PLCδ-PH-mCherry and the Ani-GFP, which marks the region undergoing constriction. These measurements were taken when the ICB reached approximately 1.5 μm in diameter. The paired mean difference between the heights of the ICB and the Ani-occupied region is shown in a Gardner-Altman estimation plot. Both groups are plotted on the left axes as a slope graph; each paired set of observations is connected by a line. The paired mean difference is plotted on floating axes on the right as a bootstrap sampling distribution. The mean difference is depicted as a dot; the 95% confidence interval is indicated by the ends of the vertical error bar.

(H) Schematic of the NSC ICB thinning zone.

Abbreviations: Ani, Anillin; ICB, intercellular bridge; MT, microtubules; NP, neural progenitor; NSC, and neural stem cell.

(I) Comparison of canonical and NSC ICB structures and thinning zones. The ICB in uncrowded cultured cells (i.e., canonical ICBs) has a tripartite organization, consisting of a midbody flanked by two arms. In contrast, the NSC ICB consists solely of a midbody with no flanking arms. While thinning occurs in the flanking arms of canonical ICBs, the NSC ICB thins at the midbody.

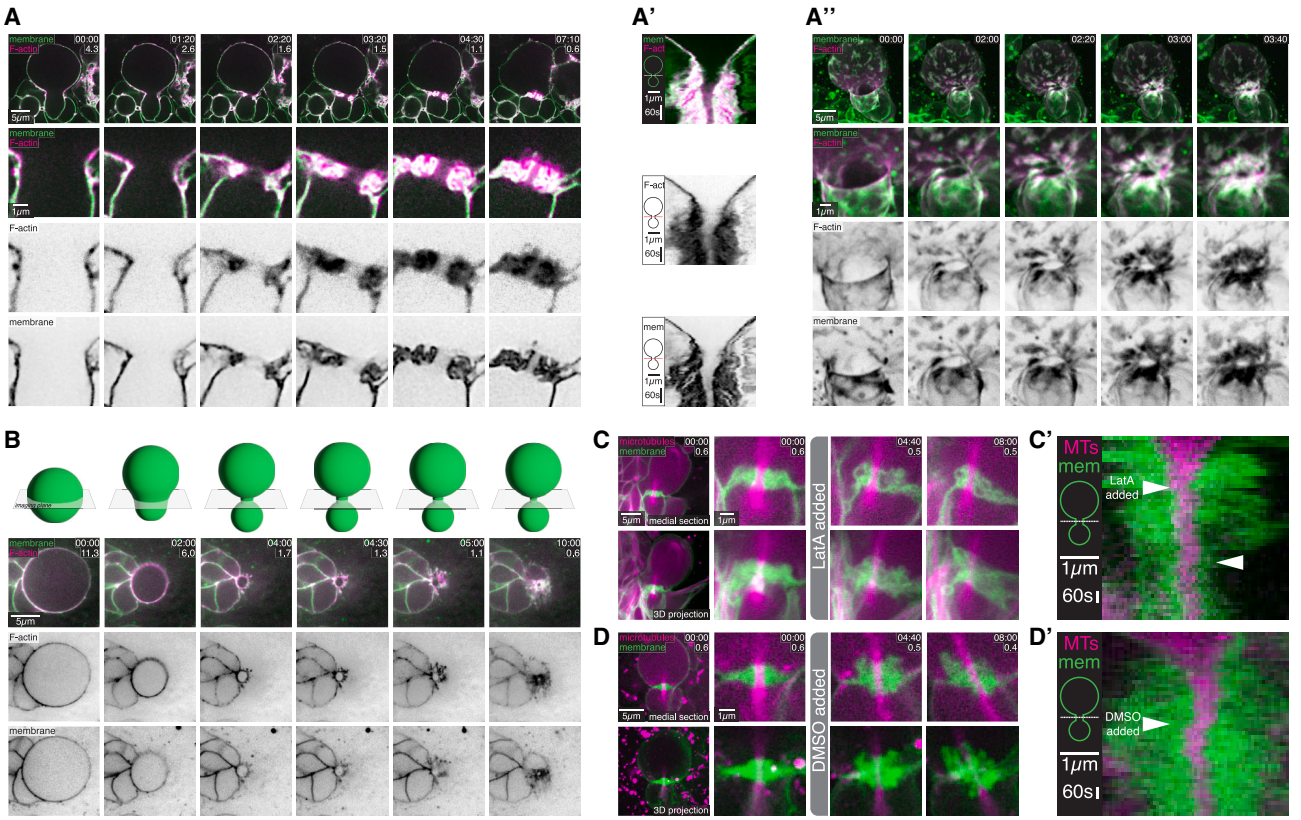


Figure 4. F-actin drives plasma membrane fluctuations as the ICB thins

(A) F-actin and membrane dynamics during the late stages of NSC division. The dynamics of F-actin (Lifeact-mRuby) and plasma membrane (PLCδ-PH-GFP) are shown in a medial section of the entire dividing NSC (top row), along with close-ups of the cleavage furrow (second, third, and fourth rows), using selected frames from Video S4. Time relative to the start of imaging is indicated (mm:ss), along with the diameter of the cleavage furrow and subsequent ICB in microns. Image deconvolution was applied. Scale bars: 5 μm (top row) and 1 μm (second, third, and fourth rows).

(A′) Kymographs of F-actin (F-act) and membrane (mem) dynamics across the ICB. Scale bars: 1 μm and 60 s.

(A″) 3D projections of F-actin and membrane dynamics during the late stages of NSC division. Dynamics of F-actin (GMA-GFP) and plasma membrane (PLCδ-PH-mCherry) are shown in 3D projection of the entire dividing NSC (top row), along with close-up views of the cleavage furrow (second, third, and fourth rows). Selected frames from Video S4 are used, with time relative to the start of imaging indicated (mm:ss). Scale bars: 5 μm (top row) and 1 μm (second, third, and fourth rows).

(B) F-actin and membrane dynamics during NSC division from a perspective looking down at the cleavage furrow and subsequent ICB as it constricts. F-actin (GMA-GFP) and plasma membrane (PLCδ-PH-mCherry) dynamics of the ICB are shown as it constricts (selected frames from Video S4). Time relative to the start of imaging is indicated (mm:ss), along with the diameter of the cleavage furrow and subsequent ICB in microns. Scale bars: 5 μm.

(C) Effects of F-actin ablation on ICB dynamics. The dynamics of microtubules (MTs) (Jupiter-mCherry) and the plasma membrane (PLCδ-PH-GFP) are shown in a medial sections (top row) and 3D projections (bottom row), with the entire dividing NSC shown in the left and a close-up view of the cleavage furrow in the remaining images (selected frames from Video S4). Latrunculin A (LatA) was added to the culture media in between the first and second frames. Scale bars: 1 μm for the left and the remaining columns.

(C′) Kymograph of MTs and membrane (mem) dynamics across the ICB. The first arrowhead indicates when LatA was added, and the second arrowhead indicates when membrane fluctuations and ICB thinning ceased. Scale bars: 1 μm and 60 s.

(D) ICB dynamics in DMSO-treated (vehicle control) NSCs. Dynamics of MTs (Jupiter-mCherry) and the plasma membrane (PLCδ-PH-GFP) are shown in medial sections (top row) and 3D projections (bottom row), with the entire dividing NSC shown in the left and a close-up view of the cleavage furrow shown in the remaining columns (selected frames from Video S4). Time relative to the start of imaging is indicated (mm:ss). DMSO was added to the culture media in between the first and second frames. Scale bars: 1 μm for the left and remaining columns.

(D′) Kymograph of MTs and mem dynamics across the ICB. The arrowhead indicates when DMSO was added. Scale bars: 1 μm and 60 s.

to the ICB. We next examined the localization of the formin Diaphanous (Dia),[36] which generates linear actin networks. While Dia was strongly enriched at the cylinder wall of the newly formed ICB (Figure 5B and Video S5), its presence was not detected in the surrounding membrane sheets. Thus, both Myosin II and Dia localize to the ICB wall but not the membrane sheets surrounding the ICB (Figure 5C).

Arp2/3-based actin networks appear during ICB formation and thinning

Given that the networks surrounding the fluctuating membrane sheets did not appear to be contractile or composed of Dia-based linear actin, we next investigated the localization of the Arp2/3 complex, which nucleates branched actin networks.[37–39] While Arp2/3 localizes to the midbody of cultured HeLa cells at

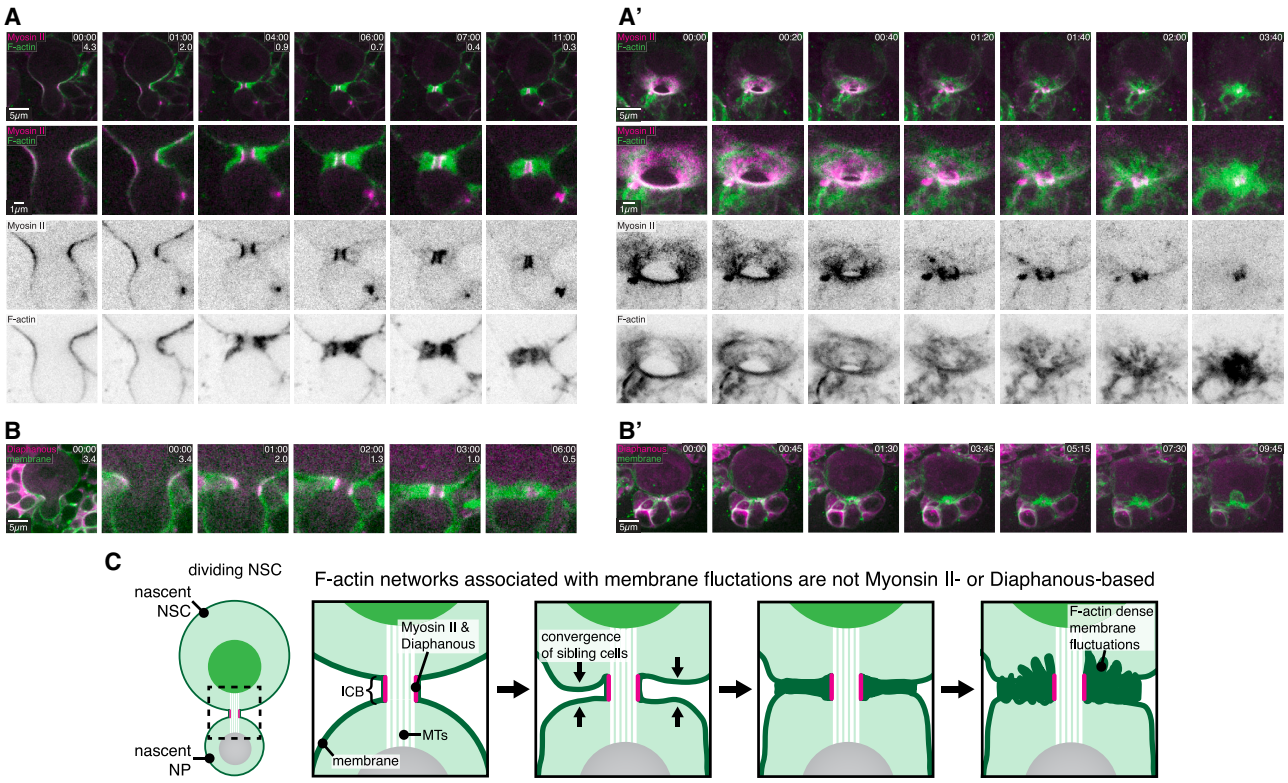


Figure 5. The actin networks of ICB-associated membrane fluctuations are not based on Myosin II or Diaphanous

(A) Myosin II and F-actin dynamics during the late stages of NSC division. The dynamics of Myosin II-GFP and F-actin (Lifeact-mRuby) are shown in medial sections (top row) and 3D projections (second, third, and fourth rows), with the entire dividing NSC shown in the left, and a close-up view of the cleavage furrow shown in the remaining images (selected frames from Video S5). Time relative to the start of imaging is indicated (mm:ss), along with the diameter of the cleavage furrow and subsequent ICB in microns. Scale bars: 5 μm (top row) and 1 μm (second, third, and fourth rows).

(A′) 3D projections of Myosin II and F-actin dynamics during the late stages of NSC division for the entire dividing NSC (top row) and close-ups of the cleavage furrow (second, third, and fourth rows), using selected frames from Video S5, with time relative to the start of imaging indicated (mm:ss). Scale bars: 5 μm (top row) and 1 μm (second, third, and fourth rows).

(B) Dynamics of the formin Diaphanous (Dia) and plasma membrane during the late stages of NSC asymmetric division. The dynamics of Dia-GFP and plasma membrane (PLCδ-PH-mCherry) are shown in medial section for the entire dividing NSC (first image), and a close-up view of the cleavage furrow is shown in the following images, using selected frames from Video S5. Time relative to the start of imaging is indicated (mm:ss), along with the diameter of the cleavage furrow and subsequent ICB in microns. Scale bars: 5 μm.

(B′) 3D projections of Dia and membrane dynamics during the late stages of NSC division, using selected frames from Video S5. Scale bars: 5 μm.

(C) Schematic of Myosin II and Dia localization during ICB formation and thinning. Both proteins localize to the ICB walls but not to the actin surrounding the dynamic plasma membrane structures that form near the ICB.

Abbreviations: ICB, intercellular bridge; MTs, microtubules; NP, neural progenitor; NSC, neural stem cell.

the completion of ICB constriction,[19] its rapidly recruitment to the furrow was observed during formation of the NSC ICB as the nascent sibling cells converged (Figures 6A and 6B; Video S6). Additionally, Arp3 co-localized with the membrane sheets and the associated F-actin networks during ICB thinning. Comparing Arp2/3, Myosin II, and Dia localization within membrane sheets adjacent to the ICB revealed that Arp2/3 is significantly enriched in this region (Figure 6D).

While Arp2/3 only weakly nucleates actin filament assembly on its own, binding to activators can dramatically enhance its activity.[40] The Arp2/3-activating SCAR complex (also known as the WAVE complex) localizes to the late cleavage furrow in NSCs,[35] suggesting that it could localize to the membrane fluctuations surrounding the ICB. We imaged the Sra1 subunit of the SCAR complex and found that it displayed similar localization patterns to Arp2/3, appearing at the cleavage furrow as it was remodeled into the ICB (Figure 6C and Video S6). The co-localization of Arp2/3 and the SCAR complex to the ICB-associated plasma membrane fluctuations suggests that Arp2/3-based actin networks drive plasma membrane remodeling during ICB formation and thinning (Figure 6E).

Arp2/3's involvement in ICB-associated membrane fluctuations and efficient ICB thinning

We next tested whether Arp2/3 is essential for the plasma membrane fluctuations near the ICB. First, we examined NSCs expressing RNAi directed against the Arpc2 subunit of the Arp2/3 complex, expressed using a tissue-specific NSC driver. These cells exhibited a noticeable reduction in the formation of plasma membrane sheets near the ICB that resulted in a significant

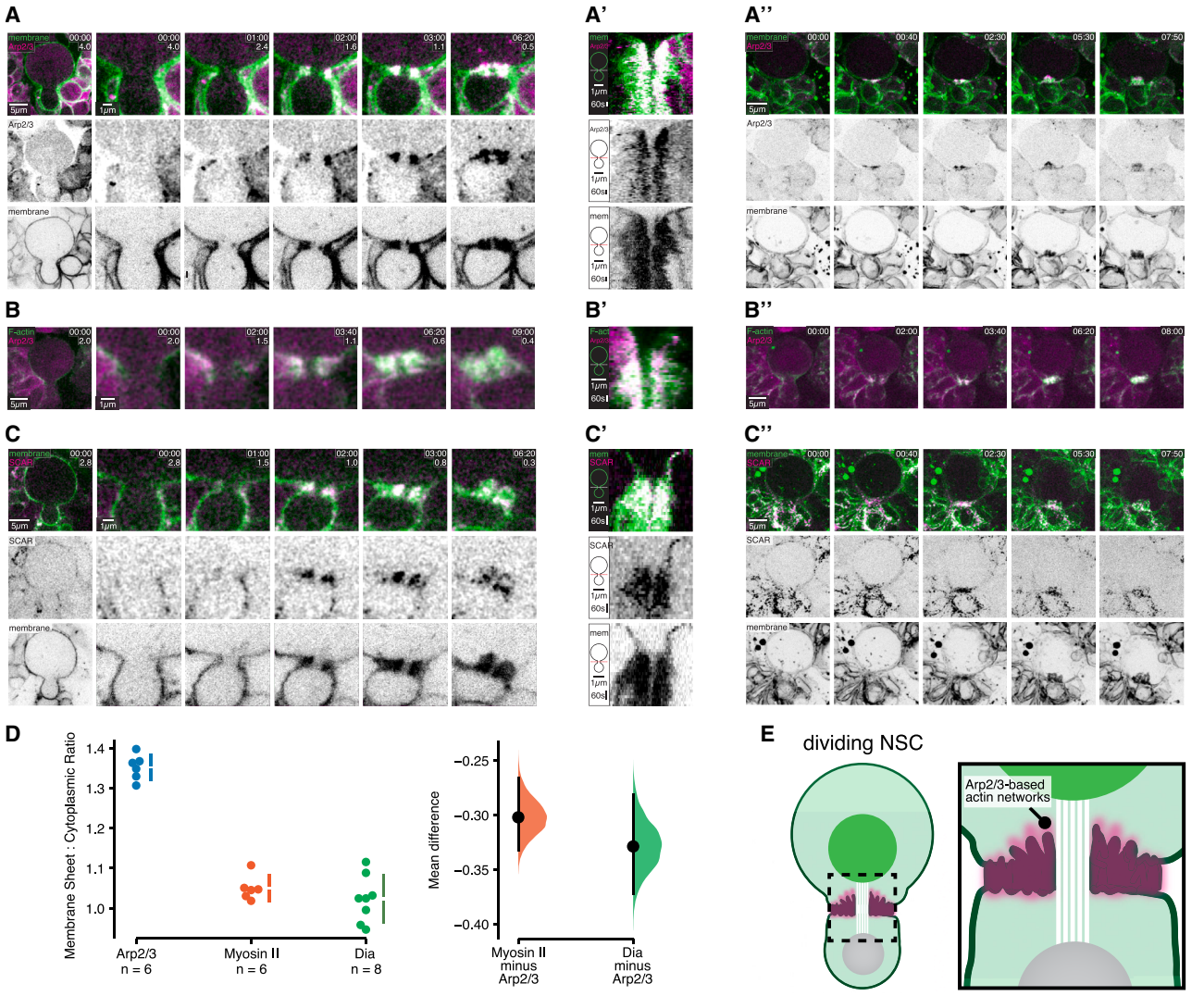


Figure 6. Arp2/3 localizes to sites of plasma membrane dynamics during ICB formation and constriction

(A) Arp2/3 complex and membrane dynamics during the late stages of NSC division. The dynamics of Arp2/3 (Arp66b-GFP) and the plasma membrane (PLCδ-PH-mCherry) are shown in medial sections of the entire dividing NSC (first image), along with close-up views of the cleavage furrow (following images), using selected frames from Video S6. Time relative to the start of imaging is indicated (mm:ss), along with the diameter of the cleavage furrow and subsequent ICB in microns. Scale bars: 5 μm (first row) and 1 μm (remaining rows).

(A′) Kymograph of Arp2/3 complex and membrane (mem) dynamics across the ICB. Scale bars: 1 μm, 60 s.

(A″) 3D projections of Arp2/3 and membrane dynamics during the late stages of NSC division, using selected frames from Video S6. Time relative to the start of imaging is indicated (mm:ss). Scale bars: 5 μm.

(B) Arp2/3 complex and F-actin dynamics during the late stages of NSC division. The dynamics of Arp2/3 (Arp66b-GFP) and F-actin (Lifeact-mRuby) are shown in medial sections of the entire dividing NSC (first image), along with close-up views of the cleavage furrow (following images), using selected frames from Video S6. Time relative to the start of imaging is indicated (mm:ss), along with the diameter of the cleavage furrow and subsequent ICB in microns. Scale bars: 5 μm (first image) and 1 μm (remaining images).

(B′) Kymograph of Arp2/3 complex and F-actin dynamics across the ICB. Scale bars: 1 μm, 60 s.

(B″) 3D projections of Arp2/3 and F-actin (F-Act) dynamics during the late stages of NSC division, using selected frames from Video S6. Time relative to the start of imaging is indicated (mm:ss). Scale bars: 5 μm.

(C) SCAR complex and membrane dynamics during the late stages of NSC division. The dynamics of SCAR-GFP and the plasma membrane (PLCδ-PH-mCherry) are shown in medial sections of the entire dividing NSC (first image), along with close-up views of the cleavage furrow (following images), using selected frames from Video S6. Time relative to the start of imaging is indicated (mm:ss), along with the diameter of the cleavage furrow and subsequent ICB in microns. Scale bars: 5 μm (first column) and 1 μm (remaining columns).

(C′) Kymograph of SCAR complex and membrane (mem) dynamics across the ICB. Scale bars: 1 μm and 60 s.

(C″) 3D projections of SCAR complex and membrane dynamics during the late stages of NSC division, using selected frames from Video S6. Time relative to the start of imaging is indicated (mm:ss). Scale bars: 5 μm.

(legend continued on next page)

decrease in the amount of plasma membrane that accumulated around the ICB (Figures 7A–7C and Video S7) and a decrease in the rate of ICB constriction (Figure 7D, $n = 5$; $N = 2$). We treated NSCs with a chemical inhibitor, CK-666,[41] to attempt to more completely abolish ICB membrane dynamics and acutely inhibit Arp2/3. The addition of CK-666 prior to ICB formation (Figures 7E–7I and Video S7) disrupted the reorganization of the cleavage furrow plasma membrane into the cylindrical ICB structure and completely abrogated plasma membrane fluctuations. This treatment resulted in nearly complete reduction in plasma membrane accumulation around the ICB (Figure 7G, $n = 5$; $N = 5$). Given the specific localization of Arp2/3 to the fluctuating membrane near the ICB, and with the assumption that CK-666 specifically inhibits Arp2/3, it appears that Arp2/3 is involved in the plasma membrane fluctuations near the ICB. The pronounced effect on the plasma membrane was accompanied by a decrease in the rate of ICB constriction in CK-666-treated NSCs at modest statistical power, indicating that Arp2/3 may be involved in the constriction process. Although we did not detect an effect of CK-666 on the initial furrowing rate, we cannot exclude the possibility that its effect on ICB constriction is indirect. When CK-666 was added after the initiation of membrane sheet fluctuations and ICB formation, we observed a qualitative cessation of membrane sheet dynamics and ICB thinning (Figures 7J and 7K; Video S7). We conclude that Arp2/3 is involved in the plasma membrane fluctuations surrounding the NSC ICB and may be involved in ICB thinning (Figure 7L).

DISCUSSION

In this study, we explored a critical aspect of cytokinesis: how the ICB is thinned in cells that are part of a tissue. ICB thinning serves as a critical intermediate step between initial furrowing and the final membrane severing of abscission because initial furrowing completes when the furrow diameter is 1.5 μm[2,4,5] but abscission requires a diameter of 200 nm.[42–46] While ICB thinning has primarily been studied in uncrowded cultured cells,[4,5,7,47,48] we investigated the process in the crowded space of the *Drosophila* larval brain and found that NSC ICB thins at the midbody because it lacks flanking arms. Concomitant with the formation and thinning of the ICB, plasma membrane fluctuations surround the ICB. The actin filament nucleator Arp2/3 complex is involved in producing these fluctuations and potentially in the ICB constriction process.

We discovered a key structural difference between canonical and NSC ICBs: while canonical ICBs are long with a central midbody surrounded by flanking arms, NSC ICBs are much shorter and consist solely of the midbody region. This difference is important because canonical ICB thinning takes place at the flanking arms. NSC ICBs appear to have adapted to this difference in structure by thinning at the midbody region. We found, through careful analysis of midbody markers combined with plasma membrane visualization, that the NSC ICBs lack flanking arms, and to our knowledge, similar analyses have not been reported in other cell types. Future work could explore whether this feature is common in cells where the nascent sibling cells stay close during division.[49–51] Canonical ICBs are long and thin because the nascent siblings migrate away from one another. We found that the nascent siblings of dividing NSCs compress against each other, with the ICB embedded within the interface between them. A previous study found that adhesions between sibling cells are necessary to maintain tissue structure.[29] In dividing NSCs where sibling cell adhesion was disrupted due to the lack of E-cadherin, the tissue became disorganized because the sibling cells no longer remained closely bound to each other.[29] Thus, in addition to the mechanical constraints of residing in the larval brain, the morphological dynamics of late NSC cytokinesis may be influenced by the cell-cell adhesions that are essential for maintaining overall tissue integrity. Intriguingly, Arp2/3 is involved in regulating adherens junction formation in epithelial cells through activity near the midbody.[52]

We also discovered that NSC ICB formation and thinning are associated with dynamic plasma membrane fluctuations, driven by Arp2/3-mediated branching of actin networks. This is in addition to its previously described roles in division, during ring canal function in germ cell division,[53–55] and polarity and fate determinant distribution during the division of the *C. elegans* zygote.[56,57] Furthermore, large plasma membrane accumulations have been observed late in cytokinesis in cells that divide in uncrowded environments,[5,9,30,33–35,50] suggesting that Arp2/3-driven membrane remodeling could be more generally utilized during late cytokinesis. It is important to note that our data do not conclusively demonstrate that the membrane fluctuations generated by Arp2/3 are responsible for ICB thinning, as Arp2/3 could play other roles in the thinning process. Furthermore, other force-generation mechanisms, such as actomyosin, play a role in ICB constriction.[47] Further work will be necessary to dissect Arp2/3's roles in ICB-associated membrane fluctuations and constriction.

What might be the role of Arp2/3-driven plasma membrane dynamics near the NSC ICBs? Tension across ICBs is carefully regulated, and abscission can require transitioning from high to low tension.[7,46] In uncrowded cultured cells, tension generated across ICBs by the migration of the nascent siblings away from one another is thought to play a critical role in thinning of the flanking arms.[4,5,7,47,48] The nascent siblings of an NSC division move toward one another, indicating that any tension across the NSC ICB is not generated in the same manner as in uncrowded cultured cells. However, large-scale membrane dynamics that take place near the ICBs suggest an intriguing alternate mechanism for tension generation across ICBs. The Arp2/3-driven plasma membrane remodeling we observed

(D) Arp2/3 is enriched in membrane sheets adjacent to the ICB. Dividing NSCs expressing Arp3-GFP ($n = 6$; $N = 5$), Myosin II-GFP ($n = 6$; $N = 5$), and Diaphanous (Dia)-GFP ($n = 8$; $N = 6$) were analyzed. Mean fluorescent intensities were measured within a region of interest in the membrane sheets adjacent to the ICB and in the neighboring cytoplasm to calculate the membrane sheet:cytoplasmic ratio. These ratios reveal that Arp2/3 was enriched within the membrane sheets, whereas Myosin II and Dia were not. The mean differences for the two comparisons against the shared control Arp2/3 are shown next to the Cumming estimation plot, with 95% confidence intervals and the bootstrap sampling distributions used to derive them.
(E) Schematic of Arp2/3-based actin networks that accompany the plasma membrane fluctuations near the ICB during its formation and constriction.

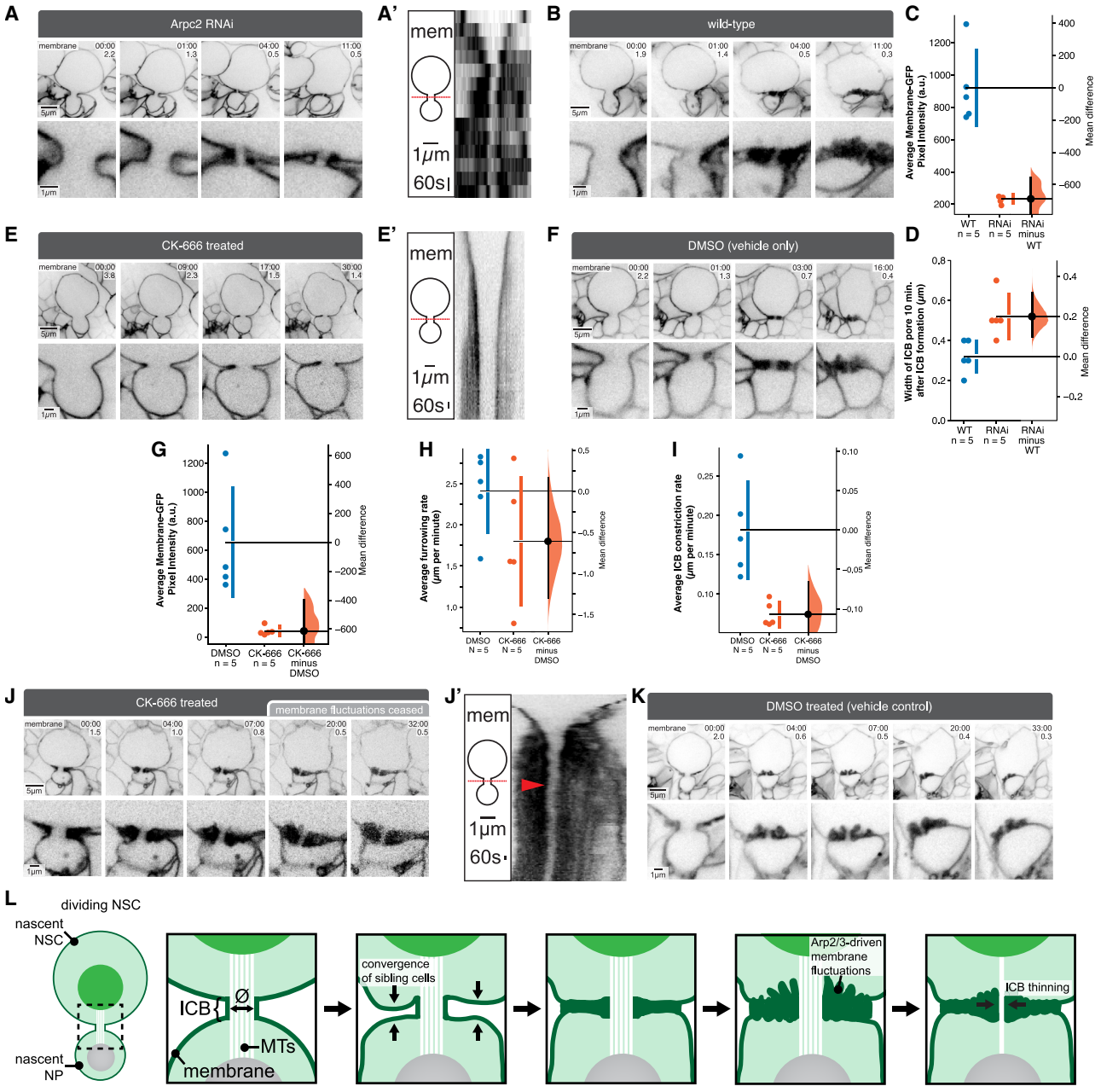


Figure 7. The Arp2/3 complex is involved in plasma membrane fluctuations and may participate in ICB constriction

(A) Arp2/3 knockdown using RNAi significantly reduces plasma membrane dynamics during the late stages of NSC division. The dynamics of the plasma membrane (PLCδ-PH-GFP) are shown in an NSC expressing Worniu-GAL4-driven RNAi against the Arpc2 subunit of Arp2/3. Selected frames from Video S7 are used to show medial sections of the entire dividing NSC (top row) and close-up views of the cleavage furrow (bottom row). Time relative to the start of imaging is indicated (mm:ss), along with the diameter of the cleavage furrow and subsequent ICB in microns. Scale bars: 5 μm (top row) and 1 μm (bottom row).

(A′) Kymograph of membrane (mem) dynamics across the ICB for the Arpc2 RNAi-expressing NSC. Scale bars: 1 μm and 60 s.

(B) The same as in (A), except the NSC is expressing no RNAi (no RNAi control). Selected frames from Video S7 are used to show medial sections of the entire dividing NSC (top row) and close-up views of the cleavage furrow (bottom row). Scale bars: 5 μm (top row) and 1 μm (bottom row).

(C) Arp2/3 knockdown via RNAi significantly reduces plasma membrane accumulation around the ICB during late NSC cytokinesis. NSCs expressing Worniu-GAL4-driven RNAi against the Arpc2 subunit of the Arp2/3 complex and the membrane marker PLCδ-PH-GFP were analyzed. The GFP signal intensity (arbitrary units) surrounding the ICB was measured 10 min after anaphase onset. NSCs expressing Arpc2 RNAi ($n = 5$; $N = 2$) and control NSCs (no RNAi, $n = 5$; $N = 2$) were compared, with the mean and standard deviation of each shown. The mean difference between the two groups is shown in the Gardner-Altman estimation plot, along with the 95% confidence interval and the bootstrap sampling distribution from which it is derived.

(D) Effect of Arp2/3 knockdown via RNAi on ICB constriction in NSCs. NSCs expressing Worniu-GAL4-driven RNAi against the Arpc2 subunit of the Arp2/3 complex and the membrane marker PLCδ-PH-GFP were used to measure the rate of ICB thinning. The diameter of the ICB, measured at 10 min after ICB

(legend continued on next page)

leads to significant membrane accumulation near ICBs, which is likely to generate pulling forces on the nearby membrane. Consistent with this possibility, Arp2/3 generates membrane tension during diverse membrane remodeling processes like endocytosis, phagocytosis, cell motility, wound healing, and cellularization.[56,58–70]

Limitations of the study

We found that Arp2/3 is involved in membrane fluctuations near the ICBs of *Drosophila* NSCs and may be involved in ICB thinning. While the inhibition of Arp2/3 with CK-666 prior to ICB formation resulted in reduced membrane fluctuations and a modest decrease in the rate of ICB constriction, a direct causal link between Arp2/3-driven membrane fluctuations and ICB thinning could not be established. It is possible that Arp2/3 contributes to thinning through the mechanisms independent of membrane fluctuations we observed. The generality of our findings will depend on what is found in other systems, both within the fly and in other organisms. We used perturbations to reduce Arp2/3 activity, and the conclusion that Arp2/3 is involved in producing ICB-associated membrane fluctuations and ICB thinning depends on the specificity of these perturbations. While CK-666 was not found to detectably affect initial furrowing rates, off-target or pleiotropic effects cannot be excluded, particularly given that Arp2/3 was inhibited or depleted prior to ICB formation in the quantified experiments. The post-ICB inhibitor experiments (Figures 7J–7L), which provide the most temporally resolved evidence, remain qualitatively assessed with a limited sample size, and, thus, the effects of acute Arp2/3 inhibition on ICB thinning after bridge formation are not yet conclusively established. The observed delays in ICB constriction upon Arp2/3 perturbation, while consistent, are moderate, and all cells in the quantified datasets ultimately underwent thinning to approximately 0.4 μm, raising the possibility that the effects may represent a delay rather than a fundamental impairment of the thinning process. We used larval central nervous system explants as a model system, and our conclusions depend on the assumption that NSCs in the cultured explants behave similarly to those *in situ*. Future studies with direct measurements of membrane tension and force generation will be needed to determine the precise mechanistic relationship between Arp2/3 activity, membrane fluctuations, and ICB thinning.

RESOURCE AVAILABILITY

Lead contact

Further information and requests for resources and reagents should be directed to and will be fulfilled by the lead contact, Kenneth E. Prehoda (prehoda@uoregon.edu).

formation, was compared between NSCs expressing Arpc2 RNAi ($n = 5$; $N = 2$) and control NSCs (no RNAi, $n = 5$; $N = 2$), with the mean and standard deviation of each shown. The mean difference between the two groups is shown in the Gardner-Altman estimation plot, along with the 95% confidence interval and the bootstrap sampling distribution from which it is derived.

(E) Effect of chemical inhibition of Arp2/3 on membrane dynamics during the late stages of NSC division. The dynamics of the plasma membrane (PLCδ-PH-GFP) are shown in an NSC treated with the Arp2/3 inhibitor CK-666 before the formation of the ICB. Selected frames from Video S7 are used to show medial sections of the entire dividing NSC (top row) and close-up views of the cleavage furrow (bottom row). We note that this cell was an outlier in terms of stalling diameter, with most others continuing to approximately 0.4 μm. Time relative to the start of imaging is indicated (mm:ss), along with the diameter of the cleavage furrow and subsequent ICB in microns. Scale bars: 5 μm (top row) and 1 μm (bottom row).

(E′) Kymograph of membrane (mem) dynamics across the ICB for the CK-666-treated NSC. Scale bars: 1 μm and 60 s.

(F) The same as in (E), except the NSC was treated with vehicle alone (DMSO) before the formation of the ICB. Selected frames from Video S7 are used to show medial sections of the entire dividing NSC (top row) and close-up views of the cleavage furrow (bottom row). Scale bars: 5 μm (top row) and 1 μm (bottom row).

(G) Effect of chemical inhibition of Arp2/3 on membrane accumulation around the ICB during late cytokinesis. NSCs expressing the membrane marker PLCδ-PH-GFP were treated with 2 mM of the Arp2/3 inhibitor CK-666 or DMSO alone before ICB formation. The GFP signal intensity (arbitrary units) surrounding the ICB was measured 10 min after anaphase onset. CK-666-treated NSCs ($n = 5$; $N = 5$) and DMSO-treated NSCs ($n = 5$; $N = 5$) are compared, with the mean and standard deviation of each shown. The mean difference between the two groups is shown in the Gardner-Altman estimation plot, along with the 95% confidence interval and the bootstrap sampling distribution from which it is derived.

(H) Effect of Arp2/3 complex inhibition on the average rate of NSC initial furrowing. NSCs expressing the membrane marker PLCδ-PH-GFP were used to measure the average of initial furrowing when treated with CK-666 or vehicle alone (DMSO). The average rate of furrowing from a furrow diameter of approximately 8–2.5 μm in CK-666-treated NSCs ($n = 5$; $N = 5$) and DMSO-treated NSCs ($n = 5$; $N = 5$) are compared, with the mean and standard deviation of each shown. The mean difference between the two groups is shown in the Gardner-Altman estimation plot, along with the 95% confidence interval and the bootstrap sampling distribution from which it is derived.

(I) Effect of Arp2/3 inhibition on NSC ICB constriction. NSCs expressing the membrane marker PLCδ-PH-GFP were used to measure the rate of ICB thinning when treated with CK-666 or vehicle alone (DMSO). The average rate of ICB constriction, from an ICB diameter of approximately 1.4–0.4 μm, in CK-666-treated NSCs ($n = 5$; $N = 5$) and DMSO-treated NSCs ($n = 5$; $N = 5$) are compared, with the mean and standard deviation of each shown. The mean difference between the two groups is shown in the Gardner-Altman estimation plot, along with the 95% confidence interval and the bootstrap sampling distribution from which it is derived.

(J) The same as in (E), except the NSC was treated with the Arp2/3 inhibitor CK-666 after the formation of the ICB. Scale bars: 5 μm (top row) and 1 μm (bottom row).

(J′) Kymograph of membrane (mem) dynamics across the ICB for the CK-666-treated NSC. The red arrow denotes when membrane fluctuations become inhibited. Scale bars: 1 μm and 60 s.

(K) The same as in (I), except the NSC was treated with the vehicle alone (DMSO) after the formation of the ICB. Selected frames from Video S7 are used to show medial sections of the entire dividing NSC (top row) and close-up views of the cleavage furrow (bottom row). Scale bars: 5 μm (top row) and 1 μm (bottom row).

(L) Arp2/3 complex's potential involvement in ICB plasma membrane fluctuations and thinning. Unlike the process observed in uncrowded cultured cells where the ICB thins as nascent sibling cells move apart, the nascent NSC siblings converge. Arp2/3 is involved in ICB-associated membrane fluctuations and may participate in efficient thinning.

Abbreviations: ICB, intercellular bridge; MTs, microtubules; NP, neural progenitor; NSC, neural stem cell; Ø, diameter of ICB.

Materials availability

This study did not generate new unique reagents.

Data and code availability

- Raw imaging data have been deposited at Dryad and are publicly available as of the date of publication at Dryad: https://doi.org/10.5061/dryad.tmpg4f5d1. All other data reported in this paper are available from the lead contact upon request.
- This paper does not report original code.
- Any additional information required to reanalyze the data reported in this paper is available from the lead contact upon request.

ACKNOWLEDGMENTS

We thank Sally Horne-Badovinac for the SCAR-GFP fly line. We thank Patrik Verstreken for the GRP1-PH-GFP fly line. We thank Chris Q. Doe for the Worniu-GAL4 and Jupiter-mCherry fly lines. We thank Evan Yamasaki of Evident Scientific for providing technical expertise related to super-resolution spinning disk microscopy. This work was supported by NIH grants K99GM147601, R25MH131653, R35GM127092, and R35GM136319.

AUTHOR CONTRIBUTIONS

B.L. and K.E.P. designed the experiments; B.L. performed the experiments and collected the data; B.L. and K.E.P. analyzed the data, prepared the figures, and wrote the manuscript; M.N.O. contributed to the preliminary screening of the Arpc2 RNAi line and quantifications of the CK-666 dataset; A.F. assisted with deconvolution; B.J.N. engaged in constructive dialogue that informed the overall research approach.

DECLARATION OF INTERESTS

The authors have no competing interests to declare.

STAR★METHODS

Detailed methods are provided in the online version of this paper and include the following:

- KEY RESOURCES TABLE
- EXPERIMENTAL MODEL AND STUDY PARTICIPANT DETAILS
  - Drosophila melanogaster
- METHOD DETAILS
  - Live imaging
  - Image processing and analysis
- QUANTIFICATION AND STATISTICAL ANALYSIS

SUPPLEMENTAL INFORMATION

Supplemental information can be found online at https://doi.org/10.1016/j.isci.2026.115430.

Received: July 10, 2025
Revised: October 19, 2025
Accepted: March 18, 2026
Published: March 23, 2026

REFERENCES

1. Fededa, J.P., and Gerlich, D.W. (2012). Molecular control of animal cell cytokinesis. Nat. Cell Biol. *14*, 440–447. https://doi.org/10.1038/ncb2482.
2. Green, R.A., Paluch, E., and Oegema, K. (2012). Cytokinesis in animal cells. Annu. Rev. Cell Dev. Biol. *28*, 29–58. https://doi.org/10.1146/annurev-cellbio-101011-155718.
3. Glotzer, M. (2017). Cytokinesis in Metazoa and Fungi. Cold Spring Harb. Perspect. Biol. *9*, a022343. https://doi.org/10.1101/cshperspect.a022343.
4. Mullins, J.M., and Biesele, J.J. (1977). Terminal phase of cytokinesis in D-98s cells. J. Cell Biol. *73*, 672–684. https://doi.org/10.1083/jcb.73.3.672.
5. Mullins, J.M., and Biesele, J.J. (1973). Cytokinetic activities in a human cell line: the midbody and intercellular bridge. Tissue Cell *5*, 47–61. https://doi.org/10.1016/s0040-8166(73)80005-9.
6. Mierzwa, B., and Gerlich, D.W. (2014). Cytokinetic abscission: molecular mechanisms and temporal control. Dev. Cell *31*, 525–538. https://doi.org/10.1016/j.devcel.2014.11.006.
7. Burton, K., and Taylor, D.L. (1997). Traction forces of cytokinesis measured with optically modified elastic substrata. Nature *385*, 450–454. https://doi.org/10.1038/385450a0.
8. Bendich, A., Vizoso, A.D., and Harris, R.G. (1967). Intercellular bridges between mammalian cells in culture. Proc. Natl. Acad. Sci. USA *57*, 1029–1035. https://doi.org/10.1073/pnas.57.4.1029.
9. Andrade, V., Bai, J., Gupta-Rossi, N., Jimenez, A.J., Delevoye, C., Lamaze, C., and Echard, A. (2022). Caveolae promote successful abscission by controlling intercellular bridge tension during cytokinesis. Sci. Adv. *8*, eabm5095. https://doi.org/10.1126/sciadv.abm5095.
10. Hu, C.-K., Coughlin, M., and Mitchison, T.J. (2012). Midbody assembly and its regulation during cytokinesis. Mol. Biol. Cell *23*, 1024–1034. https://doi.org/10.1091/mbc.E11-08-0721.
11. Addi, C., Presle, A., Frémont, S., Cuvelier, F., Rocancourt, M., Milin, F., Schmutz, S., Chamot-Rooke, J., Douché, T., Duchateau, M., et al. (2020). The Flemmingsome reveals an ESCRT-to-membrane coupling via ALIX/syntenin/syndecan-4 required for completion of cytokinesis. Nat. Commun. *11*, 1941. https://doi.org/10.1038/s41467-020-15205-z.
12. Vernì, F., Somma, M.P., Gunsalus, K.C., Bonaccorsi, S., Belloni, G., Goldberg, M.L., and Gatti, M. (2004). Feo, the Drosophila homolog of PRC1, is required for central-spindle formation and cytokinesis. Curr. Biol. CB *14*, 1569–1575. https://doi.org/10.1016/j.cub.2004.08.054.
13. Santos, I.C., Silva, A.M., Gassmann, R., and Carvalho, A.X. (2023). Anillin and the microtubule bundler PRC1 maintain myosin in the contractile ring to ensure completion of cytokinesis. Dev. Camb. Engl. *150*, dev201637. https://doi.org/10.1242/dev.201637.
14. Zhu, C., and Jiang, W. (2005). Cell cycle-dependent translocation of PRC1 on the spindle by Kif4 is essential for midzone formation and cytokinesis. Proc. Natl. Acad. Sci. USA *102*, 343–348. https://doi.org/10.1073/pnas.0408438102.
15. Mollinari, C., Kleman, J.-P., Jiang, W., Schoehn, G., Hunter, T., and Margolis, R.L. (2002). PRC1 is a microtubule binding and bundling protein essential to maintain the mitotic spindle midzone. J. Cell Biol. *157*, 1175–1186. https://doi.org/10.1083/jcb.200111052.
16. Pavicic-Kaltenbrunner, V., Mishima, M., and Glotzer, M. (2007). Cooperative assembly of CYK-4/MgcRacGAP and ZEN-4/MKLP1 to form the centralspindlin complex. Mol. Biol. Cell *18*, 4992–5003. https://doi.org/10.1091/mbc.e07-05-0468.
17. Lekomtsev, S., Su, K.-C., Pye, V.E., Blight, K., Sundaramoorthy, S., Takaki, T., Collinson, L.M., Cherepanov, P., Divecha, N., and Petronczki, M. (2012). Centralspindlin links the mitotic spindle to the plasma membrane during cytokinesis. Nature *492*, 276–279. https://doi.org/10.1038/nature11773.
18. Kodba, S., Öztop, A., van Berkum, E., Katrukha, E.A., Iwanski, M.K., Nijenhuis, W., Kapitein, L.C., and Chaigne, A. (2025). Aurora B controls microtubule stability to regulate abscission dynamics in stem cells. Cell Rep. *44*, 115238. https://doi.org/10.1016/j.celrep.2025.115238.
19. Advedissian, T., Frémont, S., and Echard, A. (2024). Cytokinetic abscission requires actin-dependent microtubule severing. Nat. Commun. *15*, 1949. https://doi.org/10.1038/s41467-024-46062-9.

20. Penkert, R.R., LaFoya, B., Moholt-Siebert, L., Vargas, E., Welch, S.E., and Prehoda, K.E. (2024). The Drosophila neuroblast polarity cycle at a glance. J. Cell Sci. *137*, jcs261789. https://doi.org/10.1242/jcs.261789.

21. Homem, C.C.F., and Knoblich, J.A. (2012). Drosophila neuroblasts: a model for stem. Cell Biol. *139*, 4297–4310. https://doi.org/10.1242/dev.080515.

22. Cabernard, C. (2012). Cytokinesis in Drosophila melanogaster. Cytoskeleton (Hoboken). *69*, 791–809. https://doi.org/10.1002/cm.21060.

23. Roth, M., Roubinet, C., Iffländer, N., Ferrand, A., and Cabernard, C. (2015). Asymmetrically dividing Drosophila neuroblasts utilize two spatially and temporally independent cytokinesis pathways. Nat. Commun. *6*, 6551. https://doi.org/10.1038/ncomms7551.

24. Cabernard, C., Prehoda, K.E., and Doe, C.Q. (2010). A spindle-independent cleavage furrow positioning pathway. Nature *467*, 91–94. https://doi.org/10.1038/nature09334.

25. Connell, M., Cabernard, C., Ricketson, D., Doe, C.Q., and Prehoda, K.E. (2011). Asymmetric cortical extension shifts cleavage furrow position in Drosophila neuroblasts. Mol. Biol. Cell *22*, 4220–4226. https://doi.org/10.1091/mbc.E11-02-0173.

26. Roubinet, C., Tsankova, A., Pham, T.T., Monnard, A., Caussinus, E., Affolter, M., and Cabernard, C. (2017). Spatio-temporally separated cortical flows and spindle geometry establish physical asymmetry in fly neural stem cells. Nat. Commun. *8*, 1383. https://doi.org/10.1038/s41467-017-01391-w.

27. Pham, T.T., Monnard, A., Helenius, J., Lund, E., Lee, N., Müller, D.J., and Cabernard, C. (2019). Spatiotemporally Controlled Myosin Relocalization and Internal Pressure Generate Sibling Cell Size Asymmetry. iScience *13*, 9–19. https://doi.org/10.1016/j.isci.2019.02.002.

28. Montembault, E., Claverie, M.-C., Bouit, L., Landmann, C., Jenkins, J., Tsankova, A., Cabernard, C., and Royou, A. (2017). Myosin efflux promotes cell elongation to coordinate chromosome segregation with cell cleavage. Nat. Commun. *8*, 326. https://doi.org/10.1038/s41467-017-00337-6.

29. Doyle, S.E., Pahl, M.C., Siller, K.H., Ardiff, L., and Siegrist, S.E. (2017). Neuroblast niche position is controlled by Phosphoinositide 3-kinase-dependent DE-Cadherin adhesion. Dev. Camb. Engl. *144*, 820–829. https://doi.org/10.1242/dev.136713.

30. Loyer, N., and Januschke, J. (2018). The last-born daughter cell contributes to division orientation of Drosophila larval neuroblasts. Nat. Commun. *9*, 3745. https://doi.org/10.1038/s41467-018-06276-0.

31. Renshaw, M.J., Liu, J., Lavoie, B.D., and Wilde, A. (2014). Anillin-dependent organization of septin filaments promotes intercellular bridge elongation and Chmp4B targeting to the abscission site. Open Biol. *4*, 130190. https://doi.org/10.1098/rsob.130190.

32. Panagiotou, T.C., Chen, A., and Wilde, A. (2022). An anillin-CIN85-SEPT9 complex promotes intercellular bridge maturation required for successful cytokinesis. Cell Rep. *40*, 111274. https://doi.org/10.1016/j.celrep.2022.111274.

33. LaFoya, B., and Prehoda, K.E. (2021). Actin-dependent membrane polarization reveals the mechanical nature of the neuroblast polarity cycle. Cell Rep. *35*, 109146. https://doi.org/10.1016/j.celrep.2021.109146.

34. LaFoya, B., and Prehoda, K.E. (2023). Consumption of a polarized membrane reservoir drives asymmetric membrane expansion during the unequal divisions of neural stem cells. Dev. Cell *58*, 993–1003.e3. https://doi.org/10.1016/j.devcel.2023.04.006.

35. Cazzagon, G., Roubinet, C., and Baum, B. (2023). Polarized SCAR and the Arp2/3 complex regulate apical cortical remodeling in asymmetrically dividing neuroblasts. iScience *26*, 107129. https://doi.org/10.1016/j.isci.2023.107129.

36. Castrillon, D.H., and Wasserman, S.A. (1994). Diaphanous is required for cytokinesis in Drosophila and shares domains of similarity with the products of the limb deformity gene. Dev. Camb. Engl. *120*, 3367–3377. https://doi.org/10.1242/dev.120.12.3367.

37. Amann, K.J., and Pollard, T.D. (2001). The Arp2/3 complex nucleates actin filament branches from the sides of pre-existing filaments. Nat. Cell Biol. *3*, 306–310. https://doi.org/10.1038/35060104.

38. Mullins, R.D., Heuser, J.A., and Pollard, T.D. (1998). The interaction of Arp2/3 complex with actin: Nucleation, high affinity pointed end capping, and formation of branching networks of filaments. Proc. Natl. Acad. Sci. USA *95*, 6181–6186. https://doi.org/10.1073/pnas.95.11.6181.

39. Volkmann, N., Amann, K.J., Stoilova-McPhie, S., Egile, C., Winter, D.C., Hazelwood, L., Heuser, J.E., Li, R., Pollard, T.D., and Hanein, D. (2001). Structure of arp2/3 complex in its activated state and in actin filament branch junctions. Science *293*, 2456–2459. https://doi.org/10.1126/science.1063025.

40. Higgs, H.N., and Pollard, T.D. (2001). Regulation of actin filament network formation through ARP2/3 complex: activation by a diverse array of proteins. Annu. Rev. Biochem. *70*, 649–676. https://doi.org/10.1146/annurev.biochem.70.1.649.

41. Hetrick, B., Han, M.S., Helgeson, L.A., and Nolen, B.J. (2013). Small molecules CK-666 and CK-869 inhibit actin-related protein 2/3 complex by blocking an activating conformational change. Chem. Biol. *20*, 701–712. https://doi.org/10.1016/j.chembiol.2013.03.019.

42. Elia, N., Sougrat, R., Spurlin, T.A., Hurley, J.H., and Lippincott-Schwartz, J. (2011). Dynamics of endosomal sorting complex required for transport (ESCRT) machinery during cytokinesis and its role in abscission. Proc. Natl. Acad. Sci. USA *108*, 4846–4851. https://doi.org/10.1073/pnas.1102714108.

43. Schiel, J.A., Simon, G.C., Zaharris, C., Weisz, J., Castle, D., Wu, C.C., and Prekeris, R. (2012). FIP3-endosome-dependent formation of the secondary ingression mediates ESCRT-III recruitment during cytokinesis. Nat. Cell Biol. *14*, 1068–1078. https://doi.org/10.1038/ncb2577.

44. Guizetti, J., Schermelleh, L., Mäntler, J., Maar, S., Poser, I., Leonhardt, H., Müller-Reichert, T., and Gerlich, D.W. (2011). Cortical constriction during abscission involves helices of ESCRT-III-dependent filaments. Science *331*, 1616–1620. https://doi.org/10.1126/science.1201847.

45. Lata, S., Schoehn, G., Jain, A., Pires, R., Piehler, J., Gottlinger, H.G., and Weissenhorn, W. (2008). Helical structures of ESCRT-III are disassembled by VPS4. Science *321*, 1354–1357. https://doi.org/10.1126/science.1161070.

46. Lafaurie-Janvore, J., Maiuri, P., Wang, I., Pinot, M., Manneville, J.-B., Betz, T., Balland, M., and Piel, M. (2013). ESCRT-III assembly and cytokinetic abscission are induced by tension release in the intercellular bridge. Science *339*, 1625–1629. https://doi.org/10.1126/science.1233866.

47. Wang, K., Wloka, C., and Bi, E. (2019). Non-muscle Myosin-II Is Required for the Generation of a Constriction Site for Subsequent Abscission. iScience *13*, 69–81. https://doi.org/10.1016/j.isci.2019.02.010.

48. Dix, C.L., Matthews, H.K., Uroz, M., McLaren, S., Wolf, L., Heatley, N., Win, Z., Almada, P., Henriques, R., Boutros, M., et al. (2018). The Role of Mitotic Cell-Substrate Adhesion Re-modeling in Animal Cell Division. Dev. Cell *45*, 132–145.e3. https://doi.org/10.1016/j.devcel.2018.03.009.

49. Carim, S.C., Kechad, A., and Hickson, G.R.X. (2020). Animal Cell Cytokinesis: The Rho-Dependent Actomyosin-Anilloseptin Contractile Ring as a Membrane Microdomain Gathering, Compressing, and Sorting Machine. Front. Cell Dev. Biol. *8*, 575226. https://doi.org/10.3389/fcell.2020.575226.

50. Alonso-Matilla, R., Lam, A.R., and Miettinen, T.P. (2024). Cell-intrinsic mechanical regulation of plasma membrane accumulation at the cytokinetic furrow. Proc. Natl. Acad. Sci. USA *121*, e2320769121. https://doi.org/10.1073/pnas.2320769121.

51. König, J., Frankel, E.B., Audhya, A., and Müller-Reichert, T. (2017). Membrane remodeling during embryonic abscission in Caenorhabditis elegans. J. Cell Biol. *216*, 1277–1286. https://doi.org/10.1083/jcb.201607030.

52. Herszterg, S., Leibfried, A., Bosveld, F., Martin, C., and Bellaiche, Y. (2013). Interplay between the dividing cell and its neighbors regulates

adherens junction formation during cytokinesis in epithelial tissue. Dev. Cell *24*, 256–270. https://doi.org/10.1016/j.devcel.2012.11.019.

53. Thestrup, J., Tipold, M., Kindred, A., Stark, K., Curry, T., and Lewellyn, L. (2020). The Arp2/3 complex and the formin, Diaphanous, are both required to regulate the size of germline ring canals in the developing egg chamber. Dev. Biol. *461*, 75–85. https://doi.org/10.1016/j.ydbio.2020.01.007.
54. Hudson, A.M., and Cooley, L. (2002). A subset of dynamic actin rearrangements in Drosophila requires the Arp2/3 complex. J. Cell Biol. *156*, 677–687. https://doi.org/10.1083/jcb.200109065.
55. Greenbaum, M.P., Ma, L., and Matzuk, M.M. (2007). Conversion of midbodies into germ cell intercellular bridges. Dev. Biol. *305*, 389–396. https://doi.org/10.1016/j.ydbio.2007.02.025.
56. Shivas, J.M., and Skop, A.R. (2012). Arp2/3 mediates early endosome dynamics necessary for the maintenance of PAR asymmetry in Caenorhabditis elegans. Mol. Biol. Cell *23*, 1917–1927. https://doi.org/10.1091/mbc.E12-01-0006.
57. Xiong, H., Mohler, W.A., and Soto, M.C. (2011). The branched actin nucleator Arp2/3 promotes nuclear migrations and cell polarity in the C. elegans zygote. Dev. Biol. *357*, 356–369. https://doi.org/10.1016/j.ydbio.2011.07.008.
58. Balzer, C.J., James, M.L., Narvaez-Ortiz, H.Y., Helgeson, L.A., Sirotkin, V., and Nolen, B.J. (2020). Synergy between wsp1 and dip1 may initiate assembly of endocytic actin networks. eLife *9*, e60419. https://doi.org/10.7554/eLife.60419.
59. Narvaez-Ortiz, H.Y., Lynch, M.J., Liu, S.L., Fries, A., and Nolen, B.J. (2024). Both Las17-binding sites on Arp2/3 complex are important for branching nucleation and assembly of functional endocytic actin networks in S. cerevisiae. J. Biol. Chem. *300*, 105766. https://doi.org/10.1016/j.jbc.2024.105766.
60. Sun, Y., Schöneberg, J., Chen, X., Jiang, T., Kaplan, C., Xu, K., Pollard, T.D., and Drubin, D.G. (2019). Direct comparison of clathrin-mediated endocytosis in budding and fission yeast reveals conserved and evolvable features. eLife *8*, e50749. https://doi.org/10.7554/eLife.50749.
61. Velle, K.B., and Fritz-Laylin, L.K. (2020). Conserved actin machinery drives microtubule-independent motility and phagocytosis in Naegleria. J. Cell Biol. *219*, e202007158. https://doi.org/10.1083/JCB.202007158.
62. Stromberg, K.A., Spain, T., Tomlin, S.A., Powell, J., Amarillo, K.D., and Schroeder, C.M. (2023). Evolutionary diversification reveals distinct somatic versus germline cytoskeletal functions of the Arp2 branched actin nucleator protein. Curr. Biol. *33*, 5326–5339.e7. https://doi.org/10.1016/j.cub.2023.10.055.
63. Mandato, C.A., and Bement, W.M. (2003). Actomyosin Transports Microtubules and Microtubules Control Actomyosin Recruitment during Xenopus Oocyte Wound Healing. Curr. Biol. *13*, 1096–1105. https://doi.org/10.1016/S0960-9822(03)00420-2.
64. Stevenson, V., Hudson, A., Cooley, L., and Theurkauf, W.E. (2002). Arp2/3-dependent psuedocleavage furrow assembly in syncytial Drosophila embryos. Curr. Biol. *12*, 705–711. https://doi.org/10.1016/S0960-9822(02)00807-2.
65. Weiner, O.D., Servant, G., Welch, M.D., Mitchison, T.J., Sedat, J.W., and Bourne, H.R. (1999). Spatial control of actin polymerization during neutrophil chemotaxis. Nat. Cell Biol. *1*, 75–81. https://doi.org/10.1038/10042.
66. Xie, C., Jiang, Y., Zhu, Z., Huang, S., Li, W., and Ou, G. (2021). Actin filament debranching regulates cell polarity during cell migration and asymmetric cell division. Proc. Natl. Acad. Sci. USA *118*, e2100805118. https://doi.org/10.1073/pnas.2100805118.
67. Peterson, A., Bennin, D., Lasarev, M., Chini, J., Beebe, D.J., and Huttenlocher, A. (2024). Neutrophil motility is regulated by both cell intrinsic and endothelial cell ARPC1B. J. Cell Sci. *137*, jcs261774. https://doi.org/10.1242/jcs.261774.
68. Williams, A.M., Donoughe, S., Munro, E., and Horne-Badovinac, S. (2022). Fat2 polarizes the WAVE complex in trans to align cell protrusions for collective migration. eLife *11*, e78343. https://doi.org/10.7554/eLife.78343.
69. Balzer, C.J., James, M.L., Narvaez-Ortiz, H.Y., Helgeson, L.A., Sirotkin, V., and Nolen, B.J. (2020). Synergy between Wsp1 and Dip1 may initiate assembly of endocytic actin networks. eLife *9*, e60419. https://doi.org/10.7554/eLife.60419.
70. Mandato, C.A., and Bement, W.M. (2003). Actomyosin transports microtubules and microtubules control actomyosin recruitment during Xenopus oocyte wound healing. Curr. Biol. *13*, 1096–1105. https://doi.org/10.1016/s0960-9822(03)00420-2.
71. Khuong, T.M., Habets, R.L.P., Kuenen, S., Witkowska, A., Kasprowicz, J., Swerts, J., Jahn, R., van den Bogaart, G., and Verstreken, P. (2013). Synaptic PI(3,4,5)P3 is required for Syntaxin1A clustering and neurotransmitter release. Neuron *77*, 1097–1108. https://doi.org/10.1016/j.neuron.2013.01.025.
72. Royou, A., Sullivan, W., and Karess, R. (2002). Cortical recruitment of nonmuscle myosin II in early syncytial Drosophila embryos: its role in nuclear axial expansion and its regulation by Cdc2 activity. J. Cell Biol. *158*, 127–137. https://doi.org/10.1083/jcb.200203148.
73. Azuma, T., and Kei, T. (2015). Super-resolution spinning-disk confocal microscopy using optical photon reassignment. Opt. Express *23*, 15003–15011. https://doi.org/10.1364/oe.23.015003.

STAR★METHODS

KEY RESOURCES TABLE

REAGENT or RESOURCE	SOURCE	IDENTIFIER
Chemicals, peptides, and recombinant proteins		
CK-666	Cayman Chemical	Cat#29038
Latrunculin A (LatA)	Enzo	Cat#BML-T119-0100
Deposited data		
Imaging data	This paper	https://doi.org/10.5061/dryad.tmpg4f5d1
Experimental models: Organisms/strains		
Anillin (Ani)-GFP (also known as Scraps in *Drosophila*)	Bloomington *Drosophila* Stock Center (BDSC)	BDSC Cat#51348 RRID: BDSC 51348
Arpc2-RNAi (RNAi against Arpc2 subunit of the Arp2/3 complex)	Bloomington *Drosophila* Stock Center (BDSC)	BDSC Cat#62339 RRID: BDSC 62339
Arp3-GFP (Arp3 tagged with GFP, marks the Arp2/3 complex)	Bloomington *Drosophila* Stock Center (BDSC)	BDSC Cat#39722 RRID: BDSC 39722
Diaphanous-GFP	Bloomington *Drosophila* Stock Center (BDSC)	BDSC Cat#56751 RRID: BDSC 56751
Farnesyl-GFP (Farnesylated-GFP that marks the plasma membrane)	Bloomington *Drosophila* Stock Center (BDSC)	BDSC Cat#80052 RRID: BDSC 80052
GMA-GFP (F-actin marker)	Bloomington *Drosophila* Stock Center (BDSC)	BDSC Cat#31776 RRID: BDSC 31776
GRP1-PH-GFP (membrane marker that binds $PI[3,4,5]P_3$ lipids)	Patrik Verstreken Lab[71]	–
Lifeact-mRuby (F-actin marker)	Bloomington *Drosophila* Stock Center (BDSC)	BDSC Cat#35545 RRID: BDSC 35545
Nervana 2 (Nrv2)-GFP (Glia cell marker)	Bloomington *Drosophila* Stock Center (BDSC)	BDSC Cat#6828 RRID: BDSC 6828
Myosin II-GFP (GFP tagged Spaghetti squash, the regulatory light chain of non-muscle type II Myosin)	Roger Karess Lab[72]	–
Pavarotti (Pav)-GFP (centralspindlin marker)	Bloomington *Drosophila* Stock Center (BDSC)	BDSC Cat#81651 RRID: BDSC 81651
PLCδ-PH-GFP (membrane marker that binds $PI[4,5]P_2$ lipids)	Bloomington *Drosophila* Stock Center (BDSC)	BDSC Cat#39693 RRID: BDSC 39693
PLCδ-PH-mCherry (membrane marker that binds $PI[4,5]P_2$ lipids)	Bloomington *Drosophila* Stock Center (BDSC)	BDSC Cat#51658 RRID: BDSC 51658
SCAR-GFP (Sra1 tagged with GFP, marks the SCAR/WAVE complex)	Sally Horne-Badovinac Lab[68]	–
Worniu-GAL4 (NSC driver line)	Chris Q. Doe Lab	–
Jupiter-mCherry (microtubule marker)	Chris Q. Doe Lab	–

EXPERIMENTAL MODEL AND STUDY PARTICIPANT DETAILS

Drosophila melanogaster

Drosophila melanogaster was used as the experimental model organism in this study. All fly strains used are listed in the key resources table. Third-instar larvae of mixed sex were used for all experiments. Because dividing NSCs in the larval brain were the subject of study, larvae were selected at the wandering third instar stage to ensure active neuroblast proliferation. No sex-specific effects were analyzed; sex-specific differences in NSC behavior have not been systematically assessed. Flies were maintained on standard Bloomington recipe food at 25°C under a 12-h light/dark cycle. For experiments involving UAS/GAL4-driven transgene expression, crosses were performed at 29°C to enhance GAL4 activity. A Worniu-GAL4 driver line was used to drive tissue-specific expression of UAS-controlled transgenes specifically in NSCs. Stocks were obtained from the Bloomington Drosophila Stock Center

or from the laboratories indicated in the key resources table. No institutional animal protocol approval was required for *Drosophila* research at the University of Oregon, as invertebrate research is exempt from IACUC oversight under current institutional and federal guidelines.

The following fluorescently tagged transgenes were used for live imaging: membrane dynamics were imaged using UAS-GAL4 driven PLCδ-PH-GFP, PLCδ-PH-mCherry, GRP1-PH-GFP,[71] and Farnesyl-GFP. Nervana 2 (Nrv2)-GFP was used as a glial cell marker. F-actin was visualized using UAS-GAL4 driven Lifeact-mRuby and GMA-GFP. Microtubules were imaged using UAS-GAL4 driven Jupiter-mCherry. Anillin was imaged using UAS-GAL4 driven Anillin-GFP. Arp2/3 was imaged using UAS-Arp3-GFP. Centralspindlin dynamics were imaged using GFP-tagged Pavarotti (Pav) protein under control of ubiquitin regulatory sequences. The formin Diaphanous was imaged using UAS-GAL4 driven Diaphanous-GFP. The SCAR/WAVE complex was imaged using Sra1/Cyfip endogenously tagged with eGFP using CRISPR/Cas9. Myosin II was imaged using GFP-tagged Spaghetti squash, the regulatory light chain of non-muscle type II Myosin, expressed from its endogenous promoter. To knock down the Arpc2 subunit of the Arp2/3 complex in NSCs, Worniu-GAL4 was used to drive expression of Arpc2-RNAi.

METHOD DETAILS

Live imaging

To obtain brain explants, third instar *Drosophila* larvae were dissected in Schneider's Insect Media (SIM) to isolate the central nervous system. Brain explants were mounted on sterile poly-D-lysine coated 35 mm glass bottom dish (ibidi Cat#81156) containing modified minimal hemolymph-like solution (HL3.1). Brain explants were imaged using a Nikon Eclipse Ti-2 Yokogawa CSU-W1 SoRa spinning disk microscope equipped with dual Photometrics Prime BSI sCMOS cameras using a 60x H_2O objective with a numerical aperture of 1.2 (for all data except Figure 3C and the final clip in Video S3). For Figure 3C and the final clip in Video S3, brain explants were imaged using an Olympus IX-83 Yokogawa CSU-W1 SoRa spinning disk microscope equipped with dual Hamamatsu ORCA-Fusion BT sCMOS cameras using a 60x Silicone objective with a numerical aperture of 1.3. 488 nm light was used to illuminate GFP tagged proteins, and 561 nm light was used to illuminate mCherry and mRuby tagged proteins. Super resolution imaging was achieved by using SoRa (super resolution through optical photon reassignment) optics.[73] NSCs were identified by their large size, location in the central nervous system, and the use of NSC specific tissue driver lines to express fluorescent markers. Time lapse imaging of cleavage furrow and intercellular bridge dynamics in a single medial section, was achieved by refocusing the imaging plane on the medial plane of the cleavage furrow and intercellular bridge, along the apical-basal axis just before capturing each frame. Three-dimensional (3D) projections of the ICB were created using multiple optical sections (300 nm z-step size) that spanned the entire volume of the NSC ICB. All figures and videos include scale bars and timestamps (mm:ss). The videos were captured at varying frame rates, which are shown in the timestamps. Pharmacological inhibition of F-actin was achieved using 50 μM Latrunculin A (LatA) dissolved in DMSO. Pharmacological inhibition of the Arp2/3 complex was achieved using 2 mM CK-666 dissolved in DMSO. Treatment with an equivalent amount of DMSO served as the vehicle-only controls.

Image processing and analysis

Imaging data was processed using ImageJ (FIJI package). For measure the progress of cytokinesis, medial sections were used to measure the diameter of the cleavage furrow and subsequent ICB. For some movies, the bleach correction tool was used to correct for photobleaching. To reduce noise in Arp3-GFP and SCAR-GFP images and videos, Gaussian blur was applied. For Figure 3C and the corresponding movie, the timelapse image stack was imported into SVI Huygens Essential v24.10, which automatically extracted the required metadata for spinning disk SoRa deconvolution, and deconvolution was performed using Huygens Deconvolution Express with the embedding medium's refractive index manually set to 1.458 to match the sample, while all other parameters were automatically estimated by the software. For Figure 4A and its corresponding movie, image deconvolution was applied using Nikon Elements' standard 2D deconvolution mode.

QUANTIFICATION AND STATISTICAL ANALYSIS

Cleavage furrow and ICB diameter measurements: Using ImageJ, a medial optical section through the cleavage furrow and ICB was selected to assess cytokinesis progression. To measure the cleavage furrow diameter, a straight line was drawn across the furrow from one side to the other. Similarly, a straight line was drawn across the ICB from one side to the other to determine its diameter.

Figure 1F: Quantifying the distance between nascent siblings during ICB thinning. In movies from dividing NSCs expressing the membrane marker PLCδ-PH-GFP, a straight line was drawn along the division axis outside of the ICB starting at the edge of the nascent NP to the nascent NSC membrane. Distances were measured following ICB formation, at 4 6, 8, 10, and 12 min after anaphase onset (n = 5 dividing NSCs; N = 3 brains). The graph depicts the mean distances between nascent siblings, with standard deviations indicated by the shaded region around the trend line.

Figure 2C: Comparison of the height of the ICB and height of the midbody. NSCs expressing the membrane marker PLCδ-PH-mCherry and the centralspindlin marker Pavarotti (Pav)-GFP, which marks the midbody, were utilized to measure the heights of both the ICB and the midbody when the cleavage furrow reached approximately 1.5 μm in diameter. The paired mean difference between the heights of the ICB and the Pavarotti occupied region is shown for n = 9 dividing NSCs (N = 9 brains) in a Gardner-Altman

estimation plot. Both groups are plotted on the left axes as a slopegraph: each paired set of observations is connected by a line. The paired mean difference is plotted on the right with 95% confidence intervals and the bootstrap sampling distribution used to derive them.

Figure 2G: Comparison of the height of the ICB and height of the constriction zone. NSCs expressing the membrane marker PLCδ-PH-mCherry and the Anillin (Ani)-GFP, which marks the region of the ICB the undergoes thinning, were utilized to measure the heights of both the ICB and the constriction zone at ICB formation, when the cleavage furrow reached approximately 1.5 μm in diameter. The paired mean difference between the heights of the ICB and the Anillin occupied region is shown for $n = 10$ dividing NSCs ($N = 10$ brains) in a Gardner-Altman estimation plot. Both groups are plotted on the left axes as a slopegraph: each paired set of observations is connected by a line. The paired mean difference is plotted on the right with 95% confidence intervals and the bootstrap sampling distribution used to derive them.

Figure 6D: Quantification of Myosin II, Diaphanous, and Arp2/3 signal intensity within membrane sheets adjacent to ICB. NSCs expressing the membrane marker PLCδ-PH-mCherry along with Myosin II-GFP, Diaphanous (Dia)-GFP, or Arp3-GFP were analyzed. For each measurement, a medial optical section through the center of an ICB, thinned to 500 nm in diameter, was selected. A mean membrane signal intensity was measured using the membrane channel to draw a 1 μm by 1 μm region of interest within the membrane sheets adjacent to the ICB. The mean signal intensity of the actin regulator (i.e., Myosin II, Diaphanous, or Arp3) within the membrane sheet region of interest was measured. A mean cytoplasmic signal intensity was measured using the membrane channel to draw a 1 μm by 1 μm region of interest in the nascent NSC cytoplasm next to the membrane sheets. The mean signal intensity of the actin regulator (i.e., Myosin II, Diaphanous, or Arp3) within this cytoplasmic region of interest was measured. Membrane:cytoplasmic ratios for $n = 6$ Arp3-GFP ($N = 5$ brains), $n = 6$ Myosin II-GFP ($N = 5$ brains), and $n = 8$ Diaphanous-GFP labeled dividing NSCs ($N = 6$ brains) were analyzed. The mean differences for two comparisons against the shared control Arp2/3 are shown next to the Cumming estimation plot. The raw data is plotted on the left. On the right, mean differences are shown with 95% confidence intervals and the bootstrap sampling distributions used to derive them.

Figure 7C: Quantification of Arp2/3 knockdown on membrane accumulation around the ICB. NSCs expressing the membrane marker PLCδ-PH-GFP and Worniu-GAL4 driven Arpc2-RNAi ($n = 5$; $N = 2$) were compared to control NSCs (no RNAi, $n = 5$; $N = 2$). The mean GFP signal intensity (arbitrary units) within a 3 μm by 3 μm region of interest over the ICB was measured 10 min after anaphase onset, with a corresponding cytoplasmic region used for background subtraction. The mean difference between the two groups is shown in the Gardner-Altman estimation plot. The mean difference is plotted on the right with 95% confidence intervals and the bootstrap sampling distribution used to derive them.

Figure 7D: Quantification of Arp2/3 knockdown on ICB thinning. NSCs expressing the membrane marker PLCδ-PH-GFP and Worniu-GAL4 driven Arpc2-RNAi ($n = 5$; $N = 2$) were compared to control NSCs (no RNAi, $n = 5$; $N = 2$). The ICB diameter 10 min after ICB formation (frame nearest to ICB diameter of 1.5 μm) was measured. The mean difference between the two groups is shown in the Gardner-Altman estimation plot. The mean difference is plotted on the right with 95% confidence intervals and the bootstrap sampling distribution used to derive them.

Figure 7G: Quantification of Arp2/3 inhibition on membrane accumulation around the ICB. NSCs expressing the membrane marker PLCδ-PH-GFP were treated with 2 mM of the Arp2/3 inhibitor CK-666 ($n = 5$; $N = 5$) or DMSO alone ($n = 5$; $N = 5$) before ICB formation. The mean GFP signal intensity (arbitrary units) within a 3 μm by 3 μm region of interest over the ICB was measured 10 min after anaphase onset, with a corresponding cytoplasmic region used for background subtraction. The mean difference between the two groups is shown in the Gardner-Altman estimation plot. The mean difference is plotted on the right with 95% confidence intervals and the bootstrap sampling distribution used to derive them.

Figures 7H and 7I: Quantification of CK-666 treatment on initial furrowing and ICB thinning. NSCs expressing the membrane marker PLCδ-PH-GFP were treated with 2 mM of the Arp2/3 inhibitor CK-666 ($n = 5$; $N = 5$) or DMSO alone ($n = 5$; $N = 5$) before ICB formation. The average rate of initial furrowing and ICB constriction was measured by dividing the change in furrow diameter (approximately from 8 μm to 2.5 μm for initial furrowing and from 1.4 μm to 0.4 μm for ICB constriction) by the elapsed time. The mean difference between the two groups is shown in the Gardner-Altman estimation plot. The mean difference is plotted on the right with 95% confidence intervals and the bootstrap sampling distribution used to derive them.